
Real-time numerical modeling of subsea cable dynamics - Visualized in Augmented Reality

Max de Feber

Thesis paper - MSc Offshore & Dredging Engineering, Delft University of Technology.

Research conducted in collaboration with Tideway Offshore Solutions and Tilburg University.

Start of project on Monday January 16, 2017 - Defended publicly on Tuesday November 28, 2017 at 9:30 AM.

Thesis committee: Prof.dr.ir. A.P. van 't Veer (TU Delft, Chairman), Dr.ir. P.R. Wellens (TU Delft, Daily supervisor), Ir. S. Meijer (Tideway, Daily supervisor), Dr. A.A. Kana (TU Delft, External committee member).

Abstract

There lies an opportunity for significant cost savings in the installation of subsea cables in offshore wind farms which is why the current work proposes a state-of-the-art method for monitoring the cable during installation. The proposed method enables offshore crew to look through the water with the use of augmented reality. To this end a real-time numerical model of the subsea cable dynamics is developed. Relevant physics are analyzed on contribution to global cable geometry and tension for the case of shallow water cable laying, resulting in an equation of motion which is sufficiently accurate for representing the physical phenomena occurring during cable lay. An assessment of the measurements required by the model during operation is made. Consequences of modeling in real-time are identified. Discretization is done using a lumped mass method. It is shown that cable dynamics can be modeled in real-time using an explicit method and that overcoming the associated limitation on axial stiffness does not lead to inaccurate results. The developed numerical solution is validated using OrcaFlex, which is typical software for dynamic analysis of offshore marine systems. An augmented reality interface is developed, including color codes indicating the structural state of the cable. The current work enables the visualization of the real-time model in augmented reality. Successful practical implementation of the proposed innovation is associated with promising opportunities.

Keywords: Real-time modeling, lumped mass method, cable dynamics, augmented reality

1. Introduction

The total installed offshore wind capacity in Europe was 12.6 GW at the end of 2016 and is expected to grow to 66.6 GW by 2030 ($\approx 5\%$ of Europe's total electricity demand) [EWEA / Wind Europe, 2016] [EWEA, 2015]. The Levelized Cost Of Energy (LCOE) of offshore wind was approximately twice as high as other renewables like bio-power, hydro power and onshore wind power in Europe, in 2016 [REN21, 2016]. In order to make offshore wind even more competitive, helping to reach the ambitious renewable energy targets stated in [European Commission, 2016], more efficient ways of installing offshore wind farms are desirable.

Subsea cable incidents make up for 77% out of the total cost of losses associated to offshore wind farms. In the period from 2008 to 2015, 90 subsea cable incidents have occurred at an average cost of €3.9 million per incident [GCube, 2016]. This percentage is highly disproportionate to the share of subsea cables in the total capital expenditure (CAPEX) of offshore wind farms, which is only 7 to 10% [Hodge, 2014]. The majority (67%) of these subsea cable insurance claims are associated to errors made by the contractor, out of which most errors stem from the cable installation process being carried out improperly [GCube, 2016]. These facts narrow down the focus of the current thesis on the installation of subsea cables in offshore wind farms, as there lies an opportunity for significant cost savings for insurance companies and/or the installation contractors.

The exact cause of these errors made by cable lay contractors generally remains unpublished. Within Tideway's cable lay installation experience, roughly half of all cable damages is related to compromising either the cable tension or bending radius limits due to poor cable handling during installation. The phenomenon of *memory* is a frequent cause of damage. Memory can cause the cable to naturally return to its previous shape when the applied tension is not appropriate during installation.

In such a case looping can occur, which may lead to pulling the cable into a very small bending radius or even a kink. The resulting bending radius in the cable could then be below the specified Minimum Bend Radius (MBR) and this will lead to cable damage and eventually replacement [McKenna, 2012]. The highly complex internal and external nature of subsea cables is what makes the cables very sensitive components which should be handled correctly in order to avoid damage [GCube, 2016]. Hence in order to minimize the risk of compromising the cable's tension or bending radius limits, the cable's state should be monitored along its full suspended length at all times during the installation process. The current thesis focuses on monitoring the cable state during installation.

In order to monitor the cable state, data is collected and provided to the Cable Lay Supervisor (CLS) during installation: top tension, departure angle, layback length, lay speed, bathymetry data including planned and as-laid cable positions, vessel heading and various video streams from cameras at important locations on the vessel. Depending on the project a Remotely Operated Vehicle (ROV) is used, which provides a mean layback distance and video stream of the cable's Touch Down Point (TDP). Mentioned parameters are defined in Figure 1.

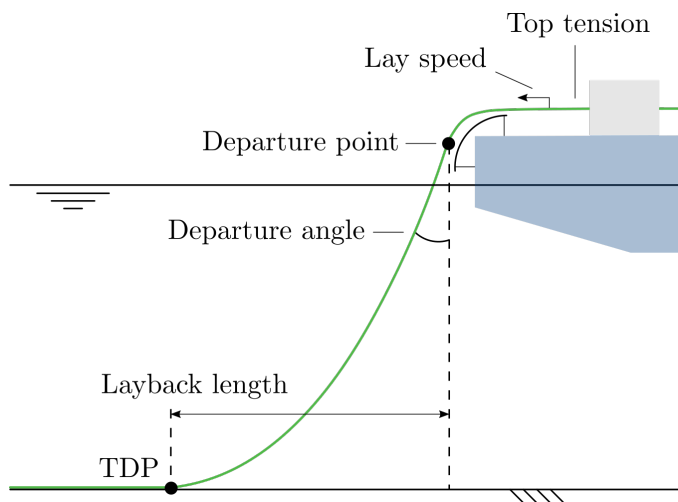


Figure 1: Key parameters for subsea cable installation.

People responsible for maintaining the cable integrity during installation are provided with all of this data through various user interfaces, mostly spread out over a multitude of computer monitors. The various sources of information are hence presented separately from each other. A typical lay-out of the working environment of a CLS is shown in Figure 2. The two monitors with white screens visible from the perspective of the CLS in Figure 2 display numerical parameters, whereas a multitude of monitors to the right (not visible from this perspective) display live streams of various video camera's. The CLS has to monitor and interpret multiple numbers and schematic visualizations simultaneously, which are displayed on different screens. Using his/her thorough knowledge and experience, the CLS combines this data in his/her mind to draw conclusions and verify the cable state. This makes judging the cable state a task which requires a high level of concentration. Due to the required knowledge and experience, only specialists are able to execute the tasks of a CLS.

To respect structural cable limits, the layback length and departure angle should be within specific ranges for specific water depths and seastates. The actual values of layback length and departure angle are typically manually compared to these

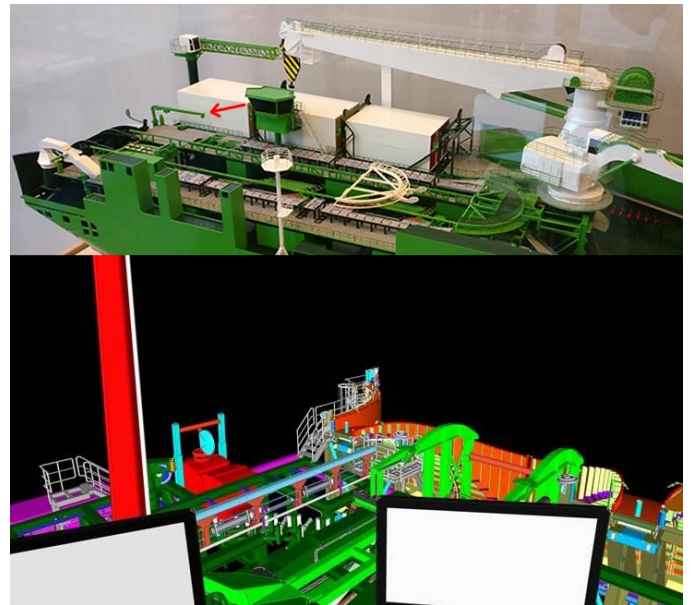


Figure 2: Working environment of a CLS. Top: CLS is located in the green control room. Bottom + red arrow: perspective from inside the control room.

specific ranges, e.g. by the CLS. This process is labour-intensive and makes assessing the operational margin between actual and limit values challenging. As typical shifts of a CLS last 12 hours per shift and are executed seven days per week for a period of three weeks, the task of monitoring and respecting key parameters during installation has to be executed for long consecutive time spans.

Thesis problem statement: “The separated nature of how various sources of data are presented to people responsible for the cable integrity during subsea cable installation does not offer an integrated overview of the operation and does not allow for instantaneous verification of the governing parameters w.r.t. related operational limits. This makes monitoring and respecting the governing parameters during installation a labour-intensive task which should only be performed by specialists and requires a high level of concentration for long time spans.”

The current work proposes an integrated visual overview of the cable laying process, which includes all relevant data about the cable at critical points along the suspended cable. The cable geometry and tension are calculated using a real-time model whose initial and boundary conditions are determined by real-time measurements. Local cable colors indicate the proximity of the current cable state to the structural limits of the cable. The structural integrity of the cable can therefore be instantly verified in real-time. During several interviews with Tideway's cable lay supervisors it was confirmed that this solution makes assessing the margin between actual and limit values easier, particularly with the use of color codes. This is an advantage especially when considering the long shifts a CLS has to make. Additionally, a more visual means of examining the under water situation makes it less challenging for both specialists and non-specialists to get an understanding of the cable lay situation. This potentially results in a wider pool of people fit for the tasks of a CLS.

Alternative methods for finding the real-time cable geometry and tension have been considered. Cable geometry could also be measured in real-time using an echoscope system onboard the cable lay vessel. An echoscope has a range of 80m to

120m [CodaOctopus, 2017a] but is typically not used for ranges above 60m for cable lay [CodaOctopus, 2017b], yielding that this method cannot be used for TDP monitoring in waters deeper than approximately 55m (assuming a layback length of 25m). In order to not be limited by water depth, the echoscope method is disregarded. Additionally, to find the cable tension a model would still be required. Another method is to attach sensors to the cable which measure and transmit position and tension. This is however deemed as highly unpractical as the cable to which the sensors are attached is being laid on the seabed. Thus the sensors would have to be collected afterwards or would be permanently lost.

Dynamic movements of the cable determine the maximum tension in the cable and the final resting configuration of the cable on the seabed [Burgess, 1993]. The proposed solution will be used to verify the structural integrity of the cable at all times, thus it is necessary to model cable dynamics. Therefore the real-time model includes cable dynamics.

Differential equations of motion describe the movements of a subsea cable. These equations are highly non-linear and generally an explicit solution is not possible [Pinto, 1995]. Only stationary cases (i.e. static or with constant relative velocity between water and cable) can be solved analytically. Thus when modeling cable dynamics a numerical solution is required.

The visual overview of the cable laying process can be displayed on a regular computer monitor. In the current thesis research, a complementary state-of-the-art way of working is explored: Augmented Reality (AR). AR is defined as the expansion of physical reality by adding layers of computer-generated information to the real environment [DHL Trend Research, 2014]. The AR status quo is given in Appendix A.4. The CLS wears an AR headset, through which the visual overview is projected as a digital layer over the physical world. When the position and shape of the subsea cable match in the digital and physical world from the point of view of the CLS, the CLS is enabled to *look through the water* and see the cable hanging from the vessel to the seabed.

Three different phases exist when installing an offshore cable between two points: first end pull-in, regular cable lay and second end pull-in. During pull-in phases the cable ends are connected to its start and end points. The current work focuses on regular cable lay, which is the phase where the vessel is sailing from start to end point and most of the total cable length is installed.

Thesis objective: “To develop a real-time numerical model of subsea cable dynamics during regular cable lay. The model should use real-time measurements as input. The results of this model are to be displayed in a real-time visual overview, which contains user-friendly color codes to help a CLS to verify the cable integrity during operation. Complementary to displaying the visual overview on a computer monitor, the overview is to be visualized in AR.”

2. Governing equations

The Equation Of Motion (EOM) of the real-time model is defined by the physics it should represent. Each typical type of physics for modeling subsea lines is assessed on its contribution to the model results, which are global cable geometry and tension. Physics which add an error smaller than the acceptable error defined in Section 2.1 to the model results when not included, are excluded from the model. Sections 2.2 to 2.13 evaluate relevant types of physics, which result in the EOM presented given in Section 2.14. The coordinate system, boundary and

initial conditions are subsequently outlined in Sections 2.15 to 2.17. The chapter ends with a plan for which measurements to use as model input in Section 2.18.

2.1. Acceptable error

A defined acceptable error for the model results is needed to assess which physics are relevant and which discretization refinement should be used (see Section 4.3). Displacement errors are acceptable when these are smaller than $0.5D$, where D is cable diameter. Tension errors are acceptable when they are smaller than 3%. Exact definitions of these errors are given in the current chapter for physics and in Sections 4.3.1 and 4.3.2 for discretization errors. The given acceptable errors are based on the author’s estimation for what is acceptable.

These acceptable errors add deviation from reality to the model results. To prevent the end-user of the model (in this case a CLS) to draw conclusions from the model results which might lead to compromising the cable’s structural limits, safety margins are added to the model results when these are presented to the end-user. These safety margins account for the made (accumulation of) model errors. The implementation of these safety margins is outlined in Section 6.

2.2. Gravity

Due to gravitational acceleration and the cable mass, a vertically downward gravity force or weight is always present. Weight governs the physical situation as it pulls the cable towards the Earth, giving it its convex curved shape. The top part of the suspended cable carries the weight of the rest of the suspended cable hanging below. The bottom part of the cable, near the TDP, carries almost no weight as there is only a small suspended cable part hanging below. Because of this principle the cable tension is highest in the top part of the suspended cable and lowest near the TDP (except for some rare and extreme dynamic cases). Therefore gravity is included in the model.

2.3. Buoyancy

Hydrostatic pressure increases linearly with water depth. Therefore when one integrates the hydrostatic pressure over the surface of a submerged body with a circular cross-section, a vertically upward force will be found: this is the buoyant force [Journee and Massie, 2001]. Another way to determine the buoyant force is to set it equal to the weight of the water that the submerged body displaces: this is Archimedes law. Buoyancy is modeled for the same reasons as those for modeling gravity. When modeling gravity and buoyancy, it is convenient to use a *submerged weight* instead of computing both forces separately. Typically the submerged weight of a cable is specified by the cable manufacturer. When it is not given by the manufacturer, the submerged weight can be calculated by subtracting the buoyancy from gravity force.

2.4. Axial stiffness

Axial stiffness or elasticity is the cable property which dictates the resistance of the cable to be stretched in axial direction. The property is indicated by the axial force required to stretch a cable element with unit length. When axial stiffness is included in a model, it is assumed that the cable is extensible and hence can be stretched. Various cable models found in literature have made different assumptions regarding axial stiffness.

According to [Faltinsen, 1990], who provided solutions for static cable analysis, the elasticity of the cable has to be included only in extreme conditions. Hence for configurations in which the cable's state stays far away from its structural limits, the influence of the elasticity of the cable on the global configuration is very small. In the work of [Pinto, 1995], dynamics of cable laying are modeled under the assumption that the cable is inextensible. Pinto's argumentation is based on the assumption of [Zajac, 1957], who also assumes that the cable is inextensible. The assumption is said to be reasonable because the cable is under relatively low tension and has a relatively high axial stiffness. Therefore only very small changes in length due to cable elasticity are expected.

More recent publications however take extensibility into account. Building on the cable dynamics model published in 1995, Pinto later published another work in which the unsteady dynamic response of submarine cables is modeled. Pinto's new work models the cable axial stiffness and thus distinguishes unstretched from stretched cable lengths [Pinto, 2007]. An exact formulation of cables undergoing axis stretching and flexural curvature has been proposed in [Lacarbonara and Pacitti, 2008].

Section 5.1 includes a comparison in cable geometry and tension for a case excluding and including axial stiffness i.e. for a case modeling the cable as inextensible and modeling the cable as stretchable. In the respective section, it is shown that the static geometry and tension errors resulting from modeling the cable as inextensible are $0.18D$ and 0.4% , respectively, for cable A (see Table 6). According to Section 2.1, these errors are acceptable.

It can be concluded that neglecting a cable's elasticity adds only a small level of inaccuracy. Recent publications account for cable elasticity, perhaps because nowadays more computational power for solving the numerical solution is available. The current work also includes axial stiffness as including it was relatively simple, no numerical problems were foreseen, provides more accuracy than assuming an inextensible cable and makes computing the cable tension a straightforward procedure.

Axial force or tension T in a cable element with axial stiffness EA which is stretched with strain ϵ , is calculated using Equation 1. Effective tension, as outlined in [DNV, 2005], is the tension used throughout the report and will from here on be referred to as tension. Typical subsea cable properties are given in Appendix A.2.2. A linear axial stiffness is assumed, as typically cable manufacturers specify only one independent value for axial stiffness. It is assumed that the Poisson effect (cross-sectional area shrinkage due to longitudinal elongation) can be neglected, as only very small elongations are expected. Furthermore, it is assumed that torsion and thus tension-torsion coupling can be neglected as explained in Section 2.12. Therefore no torque term is present in Equation 1. Additionally, as no coupling between pulling and twisting is assumed, one can define a single value for the axial stiffness of the cable (instead of different values depending on cable twist) [Zajac, 1957]. Strain ϵ can be calculated using Equation 2, where l_{ij} and l_0 are stretched and unstretched length, respectively.

$$T = EA \cdot \epsilon \quad (1) \quad \epsilon = \frac{l_{ij} - l_0}{l_0} \quad (2)$$

2.5. Hydrodynamic drag

Hydrodynamic drag on the cable can result from movements of the water and/or the cable. It is assumed that direct wave effects on the cable are small and negligible, considering the small diameter and large length of the cable. This assumption is in accordance with assumptions made in [Pinto, 2007]. As

the direct wave effects are negligible, no waves are modeled. Ocean currents are assumed to affect cable geometry and tension significantly and therefore constant currents are included in the model. This assumption is verified in Section 2.5.1.

As no waves are modeled and only constant currents are assumed, the water surrounding the cable is not accelerating. This means that the water has no ambient dynamic pressure gradient, whereby the Froude-Krilov force ($f_{FK} = \rho_w \cdot A_{cable} \cdot a_w$) is zero [Journee and Massie, 2001].

Vessel movements resulting from waves have a strong influence on the global dynamic behaviour of the cable, as the cable is fixed to the vessel. This adds significant horizontal and vertical velocities to the cable, resulting in hydrodynamic drag. Hence large cable movements may result indirectly from waves. Therefore, the indirect effect of waves through vessel motions is included.

Concluding the above: cable movements resulting from dynamic excitation of the departure point (which in turn result from vessel movements) are modeled in a water column which has a zero or constant (i.e. stationary) uniform velocity field. Hydrodynamic drag resulting from these cable movements is decomposed into normal and tangential components, which are analyzed in Sections 2.5.1 and 2.5.2.

2.5.1. Normal hydrodynamic drag

In order to assess whether the normal hydrodynamic drag force is significant enough to include in the model's physics, a static situation without current has been compared to stationary situations including various current speeds. Cases excluding and including uniform in-plane currents have been modeled using the numerical model described in Section 4.2. All properties except the current velocity are equal in the modeled cases: cable A from Table 6 with $EI = 0Nm^2$, $L = 62m$ and $d = 40m$.

It is assumed that a cable element can be modeled as a slender cylinder. A moving slender cylinder in a constant water flow will experience a quadratic drag force in normal direction, which is assumed to be caused by perpendicular relative flow velocity V_p [Journee and Massie, 2001]. Normal drag force $F_{D,n}$ can be calculated with Equation 3 where ρ is the water density, $C_{D,n}$ is the normal drag coefficient which is dependent on Reynolds number, D is the cable diameter and l is the cable section length. The perpendicular flow velocity V_p which is used throughout the model is a relative velocity, which is illustrated in Figure 3 and calculated using Equation 4, where $(\dot{x} - \dot{x}_{cur})$ is the relative horizontal movement of the cable \dot{x}_{rel} and θ is the angle between the cable longitudinal axis and the vertical. As the modeled currents only have a component in horizontal direction (i.e. $\dot{z}_{cur} = 0$), the vertical cable movement \dot{z} is equal to the relative vertical cable movement \dot{z}_{rel} . Velocity V_p is defined positive for cable movements to the right-hand side of the cable. Appendix A.1 outlines how the correct hydrodynamic normal drag sign is calculated.

$$F_{D,n} = \frac{1}{2} \cdot \rho \cdot C_{D,n} \cdot D \cdot l \cdot V_p^2 \quad (3)$$

$$V_p = (\dot{x} - \dot{x}_{cur}) \cdot \cos(\theta) - \dot{z} \cdot \sin(\theta) \quad (4)$$

Drag coefficient $C_{D,n}$ is dependent on Reynolds number Re and dimensionless surface roughness k/D . The Reynolds number is calculated using Equation 5, where U is flow velocity amplitude and ν is kinematic viscosity [Journee and Massie, 2001]. It is assumed that the magnitude of the relative normal cable element movement V_p is equal to flow velocity amplitude U and hence is used for calculating Re .

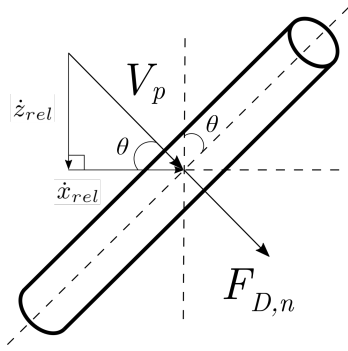


Figure 3: Definition of angle θ , velocity V_p and relative velocities \dot{x}_{rel} and \dot{z}_{rel} .

$$Re = \frac{U \cdot D}{\nu} = \frac{|V_p| \cdot D}{\nu} \quad (5)$$

The case under consideration models salt water of $10^\circ C$ which has a kinematic viscosity ν of $1.35383(10^{-6}) \text{ m}^2/\text{s}$ [Journee and Massie, 2001]. Because the surface of a subsea cable is relatively rough as shown in Figure 4, it is assumed that the surface roughness k of the modeled cable is equal to the surface roughness of highly corroded steel, yielding $k = 3 \cdot 10^{-3} \text{ m}$ [DNV GL, 2017]. This yields a dimensionless roughness k/D of $1.3 \cdot 10^{-2}$. The corresponding $C_D(Re)$ curve is given in Figure 5.



Figure 4: Subsea power export cable with $D = 0.155\text{m}$.

Figure 6 shows the stationary cable geometries resulting from various uniform in-plane currents. The currents which have been applied range from -1.5 to 2.5 m/s . Current velocities below -1.5 m/s result in inverse static catenary shapes with the used modeling setup. These inverse catenary geometries are non-existent in real cable lay operations and are hence not included. Positive current velocities are limited at 2.5 m/s because higher current velocities are rare in a typical North Sea cable lay project [Wagenaar and Eecen, 2010].

As can be verified with visual inspection in Figure 6, the normal hydrodynamic force resulting from current significantly affects the cable geometry. The layback lengths found in cases with -1.5 and 2.5 m/s differ with 15m , which equals 24.2% of the modeled cable length. Cable tension is also highly dependent on current velocity, as shown in Figure 7. The relevance of normal hydrodynamic drag is shown in Figure 8, where submerged weight is plotted next to normal hydrodynamic drag force. Because the cable geometry and tension are largely affected by the normal hydrodynamic force and because excluding normal hydrodynamic drag would lead to model errors well above the

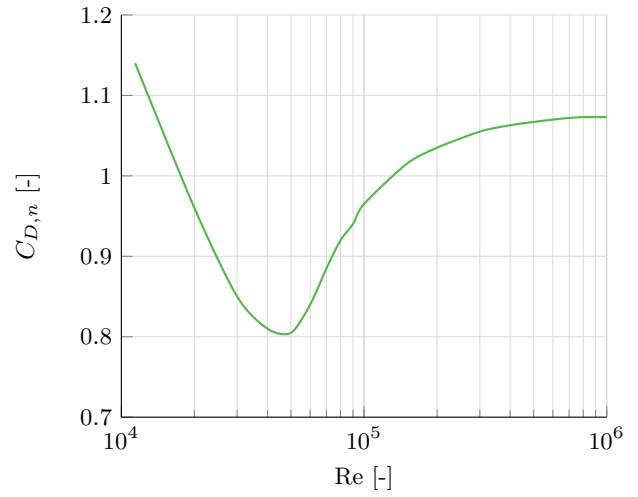


Figure 5: Drag coefficient for a fixed circular cylinder in steady flow, for dimensionless roughness k/D of 10^{-2} [DNV GL, 2017].

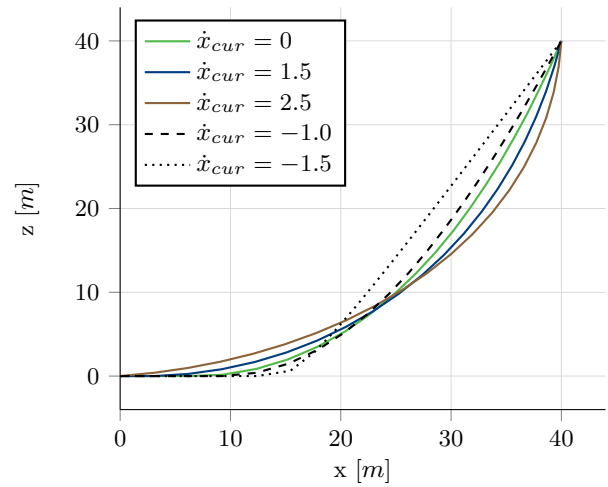


Figure 6: Stationary cable geometry for uniform in-plane currents of different magnitudes. Positive and negative velocities indicate currents towards the right and left, respectively. Velocities are given in $[\text{m/s}]$.

acceptable errors defined in Section 2.1, this force is included in the numerical model.

2.5.2. Tangential hydrodynamic drag

Literature defines different methods for computing the tangential component of hydrodynamic drag on slender structures. [Journee and Massie, 2001] mention only a quadratic drag force which acts in the normal cable axis direction, whereas [Boom, 1985] derives the total hydrodynamic drag force from both normal and tangential components. The most recent recommended practice by [DNV GL, 2017] states that the tangential drag force may be important for long slender elements with a considerable relative tangential velocity component. The recommended practice specifies three different methods for calculating the tangential drag force on inclined cylinders, but remains unclear about which method to use in the case of cables. Because no clear answer is found in literature, the relevance of tangential drag has been analyzed for the specific case of offshore cable laying in the current work.

In order to find the significance of tangential drag, the most conservative of methods found in literature has been used to

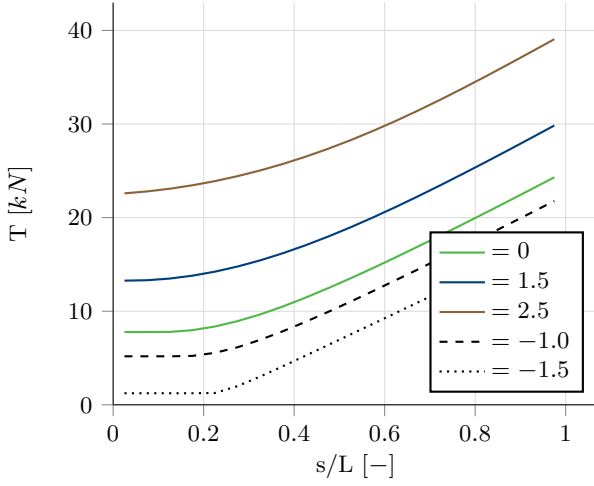


Figure 7: Stationary cable tension resulting from normal hydrodynamic drag for uniform in-plane currents of different magnitudes. Positive and negative velocities indicate currents towards the right and left, respectively. The legend gives current velocities in [m/s].

model it. This is the method provided by [Boom, 1985], in which the tangential drag is calculated in an analogous way to the normal drag. Tangential drag $F_{D,t}$ can be calculated using Equation 6.

$$F_{D,t} = \frac{1}{2} \cdot \rho \cdot C_{D,t} \cdot D \cdot l \cdot V_t^2 \quad (6)$$

The tangential drag coefficient $C_{D,t}$ is dependent on surface roughness and the angle of attack α . Following the assumption made for calculating the normal drag (i.e. the surface roughness of the modeled cable is equivalent to the surface roughness of highly corroded steel), the ratio $C_{D,t}/C_{D,n}$ has a maximum value of 0.0575 for $\alpha = 36^\circ$ [DNV, 2007]. For a conservative assessment of the significance of the tangential drag, the dependency on angle of attack will be disregarded and the most conservative normal drag coefficient from Figure 5 will be used to calculate $C_{D,t}$. This yields $C_{D,t} = 0.066$, which is indeed on the conservative side when compared to values used in other relevant works ($C_{D,t} = 0.01$ in [Pinto, 1995] and 0.03 in [Yang et al., 2013]).

The normal and tangential drag components for a stationary case with current velocity 2.5 m/s along the length of the cable are given in Figure 8. The modeled environment and cable are equal to the cases modeled in Section 2.5.1.

As can be seen in Figure 8 the tangential drag component is marginal with respect to the normal component, suggesting that tangential drag does not affect the cable geometry and tension significantly. To verify this, the stationary cable geometries for a positive uniform in-plane current of 2.5 m/s in- and excluding tangential drag have been compared. The resulting maximum absolute difference in location of the cable's nodes is less than 5cm, which equals 0.21D. As $0.21D < 0.5D$ this is an acceptable error.

The relatively low tangential drag force can be explained by several reasons. First of all, the geometry of the modeled cable has only a minor part which is horizontally orientated: this is the part on and near the seabed. Also, the tangential drag coefficient is at least twelve times smaller than the normal drag coefficient. The physical tangential drag force will be lower than the drag force as it is modeled in the current work. The modeled current is uniformly distributed over the water depth, but in

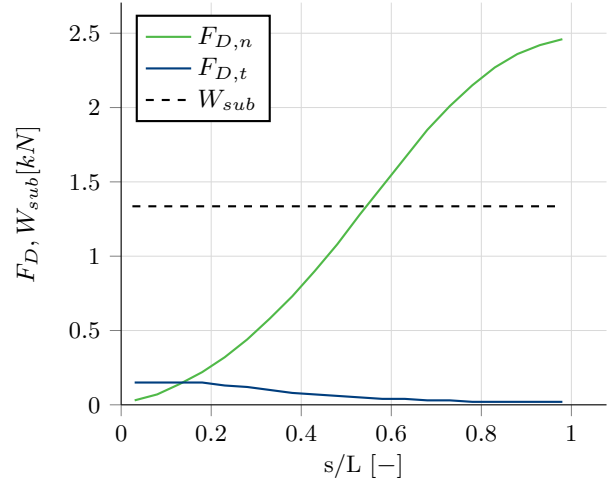


Figure 8: Normal and tangential drag force components on a stationary cable geometry for a positive uniform in-plane current of 2.5 m/s. Submerged weight W_{sub} is illustrated to show the relevance of the magnitude of the hydrodynamic drag forces.

reality the current velocity decreases near the seabed [DNV GL, 2017]. The cable part near the seabed is the part with the largest tangential velocity component of the total cable, which hence will see an even smaller tangential velocity component when a non-uniform current profile is present. Considering the above-mentioned arguments it is concluded that tangential drag does not contribute significantly to the cable geometry and tension. Therefore tangential drag is not modeled in the current work.

2.6. Cable laying

The cable laying vessel is sailing and simultaneously pays out cable, which adds two physical effects to the system: a uniform movement of the water column w.r.t. the cable (vessel sails) and an additional tangential cable velocity (cable is being laid). These physical effects are visualized in Figure 9. The impact of these phenomena on the model results are analyzed in Sections 2.6.1 and 2.6.2. The vessel velocity and lay speed are assumed to be equal while in actual cable lay operations these quantities might temporarily differ slightly from each other, when e.g. the layback length of the cable should be altered. A typical lay speed of $8 \frac{m}{min}$ ($480 \frac{m}{h}$) is assumed.

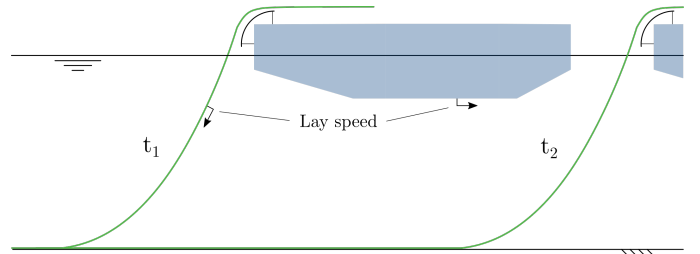


Figure 9: Cable laying: the vessel sails and the cable is being laid.

2.6.1. Vessel sails

This phenomenon can be modeled by adding a constant uniform current of $-480 \frac{m}{h}$ ($-0.133 \frac{m}{s}$) to the model. The negative sign represents the fact that the vessel is sailing in positive x -direction

hence the cable sees the water column moving in negative x -direction (coordinate system is defined in Section 2.15). As outlined in Section 2.5, this current is modeled by adding normal hydrodynamic drag to the cable, which is done for the following case: cable A from Table 6 but with $EA = 22MN$, $L = 62m$ and $d = 40m$. Stationary cable geometry and tension differences between a case without current and a case with a current of $-0.133\frac{m}{s}$ are quantified and made dimensionless. The geometry of the stationary cable with $-0.133\frac{m}{s}$ current deviates maximally with $-0.04D$ (in x -direction) from the case without current. Tensions found in the stationary cable with $-0.133\frac{m}{s}$ current are lower (which is as expected as the current acts in negative x -direction) and the maximum tension deviation is -0.92% from the tension in the case without current. As these errors are below the acceptable error defined in Section 2.1, the effect of a sailing vessel with a velocity of $8\frac{m}{min}$ is neglected.

2.6.2. Cable is being laid

Because the cable is being laid during installation, the entire cable moves in tangential direction with the lay speed of $8\frac{m}{min}$. For the case shown in Figure 8, this additional tangential velocity yields a $F_{D,t}$ increase of $0.007kN$ (at $\frac{s}{L} = 0$). As this force is only 4.3% of the already negligible tangential drag force at $\frac{s}{L} = 0$ (as outlined in Section 2.5.2), its impact on the model results is assumed to be negligible. Therefore the additional tangential drag force resulting from paying out the cable is disregarded.

2.7. Seabed

The dynamic location of the TDP is one of the model's most important results. Dynamic excitation of the cable moves the TDP around its static equilibrium position on the seabed. Therefore to model the dynamic movements of the TDP, the modeled cable should be longer than the suspended cable length in static configuration. This yields that even though the main focus of the current research lies on the suspended part of the cable, a relatively small cable part which lies on the seabed should also be modeled. The purpose of modeling the seabed is hence only to let the cable touch down and lie on a solid surface, in order to calculate the location of the TDP. Accurate soil-structure interaction is not of interest in the current work. It is assumed that the seabed is frictionless, which is in line with assumptions made in [Pinto, 1995]. The advantage of this assumption is that complex formulae for cable-seabed interaction are avoided.

As accurate soil-structure interaction is beyond the scope of the current work, a simple way elastic seabed model is used. As explained later in Section 4, the cable will be discretized using lumped mass nodes which are connected by massless elements. The simplest approach to model a flat surface at a certain vertical location z_{seabed} , is by adding an upward spring force on nodes which satisfy $z_{node} < z_{seabed}$. As the springs were undamped, the cable nodes experienced a *trampoline-effect*, which is shown with the green line in Figure 10.

This *trampoline-effect* is spurious and amplifies the tension in the surrounding cable elements, which are both undesired. Therefore viscous dampers are added to the seabed model. The purpose of the seabed model in the current work is to just let the cable touch down and lie on the seabed. The viscous dampers are therefore critically damped as critical damping gives the fastest return of the system to its equilibrium position [MIT, 2011], yielding a minimized amount of oscillations. The total seabed normal force is calculated using Equation 7 [MIT, 2011]. As shown in Figure 10, the critically damped dampers eliminate

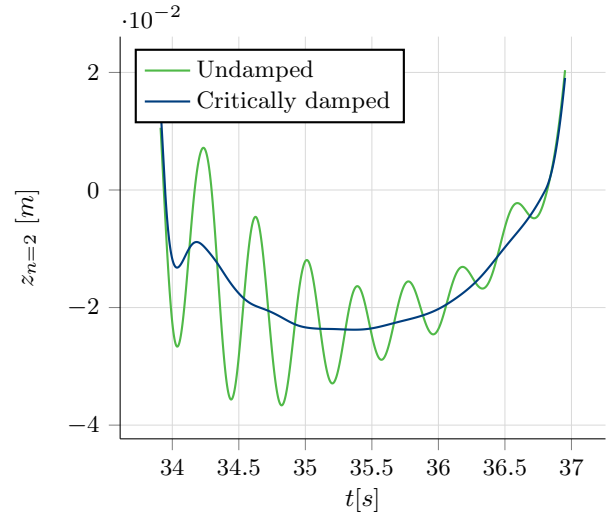


Figure 10: Vertical displacement of a cable node which is in the TDP area of a dynamically excited cable. Seabed is at $z = 0$.

the *trampoline-effect*.

$$F_{seabed} = \begin{cases} -\sqrt{Amk_s} \cdot \dot{z} - k_s \cdot z, & z < 0 \\ 0, & z \geq 0 \end{cases} \quad (7)$$

Mass m in Equation 7 equals the lumped mass on one node. Stiffness k_s is the soil stiffness, for which a value of $100\frac{kN}{m}$ is assumed. This value doesn't yield extremely high normal forces which could lead to model instability and neither it lets the cable sink into the seabed too deep (only a few centimeters, depending on cable submerged mass and amount of elements).

The above-mentioned amplification of the tension in surrounding cable elements for undamped springs and the tension with critically damped dampers is shown in Figure 11. The tension range for the tension wave period indicated with the dashed vertical lines in Figure 11 has decreased with 33.8%. The spurious tension amplification resulting from the *trampoline-effect* has thus been eliminated.

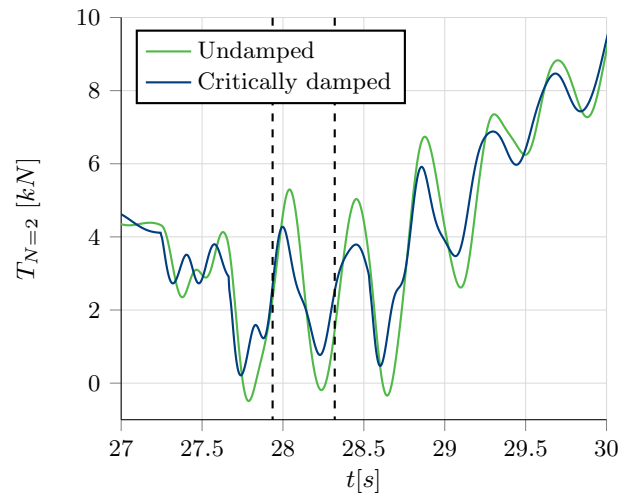


Figure 11: Tension in a cable element which is in the TDP area of a dynamically excited cable.

Setting the sum of forces in z -direction to zero when the node gets near the seabed has also been considered as an alternative to model the seabed in a simple way. However numerical challenges were expected and the condition for when the node

should be released again from the seabed is challenging to define. Therefore the presented solution with critically damped visco-elastic supports has been used.

2.8. Inertia

When considering dynamics, inertia of the physical system should be included in the model. Including inertia is done by adding the force required to accelerate the cable to the equation of motion. This force is given in Equation 8.

$$F_{inertia} = m \cdot a \quad (8)$$

2.9. Added mass

When the cable accelerates, it accelerates some of the water surrounding the cable. This phenomena adds inertia to the system and is called *added mass*. Added mass is dependent on relative acceleration between cable and water a_r , mass of the water that is displaced by the cable $\rho_w A_{cable}$ and an added mass coefficient C_A . The sectional added mass force can be calculated using Equation 9 [DNV GL, 2017].

$$F_a = C_A \cdot \rho_{fluid} \cdot A_{cable} \cdot a_r \quad (9)$$

As explained in Section 2.5, the water surrounding the cable is assumed to be not accelerating i.e. $a_{fluid} = 0$. Therefore, relative acceleration $a_r = a_{fluid} - a_{cable}$ is equal to the cable acceleration multiplied with minus one. Hence $a_r = -a_{cable}$, where the minus sign indicates that the added mass force acts in opposite direction of the cable acceleration.

For determining the added mass coefficient, the assumption is made that the modeled cable is surrounded by an infinite fluid far from boundaries. For such a submerged body, $C_A = 1$ [DNV GL, 2017]. The assumption of an infinite fluid around the cable is increasingly incorrect as the cable gets closer to boundaries like the seabed. As in the current work C_A is assumed to constantly be 1, Equation 9 can be rewritten to Equation 10 where constant scalar quantity $m_a = C_A \cdot \rho_{fluid} \cdot A_{cable}$.

$$F_a = -m_a \cdot a_{cable} \quad (10)$$

Equation 10 can be merged with Equation 8 for simplicity. This yields Equation 11, which is used in the EOM.

$$F_{inertia} = (m + m_a) \cdot a \quad (11)$$

To indicate the significance of including added mass in the model: the inertial mass of the cable as given in Equation 12 increases with 50.09%, for cable A in a fluid with $\rho = 1025 \frac{kg}{m^3}$.

$$m_{inertia} = m + m_a = \rho \cdot A + C_A \cdot \rho_w \cdot A \quad (12)$$

It is expected that C_A is not exactly 1 in actual physics for several reasons. First of all, the theoretical value of C_A is 1 and is based on a theoretical flow pattern around the cable. In practise a real instead of potential (theoretical) flow is present, in which the flow behind the cable is not laminar but has detached from the cable and became turbulent. The latter causes C_A to be usually smaller than 1 [Journee and Massie, 2001]. Additionally, vortex induced vibrations (VIV) have a large impact on C_A . As shown by [Vikestad et al., 2000] coefficient C_A ranges from (-1) to 4.5 depending on reduced velocity, which is a typical parameter for analyzing VIV behaviour. As VIV is beyond the scope of the current research, its effect on C_A is also not included.

2.10. Aerodynamic drag

As shown in Figure 1, the suspended cable is mainly surrounded by water but part of the cable (from waterline to departure point) is surrounded by air. Therefore, aerodynamic drag will be applied on this emerged cable part whenever a relative velocity between cable and air is present. The magnitude of aerodynamic drag can be calculated using Equation 3, when ρ is replaced by ρ_{air} . The ratio $\frac{\rho}{\rho_{air}}$ is approximately equal to $\frac{1025}{1.225} = 837$. Additionally, approximately only 10% of the suspended cable (hanging from touch down point to departure point) is surrounded by air. Hence when assuming equal relative water and air velocities, hydrodynamic drag is $\frac{1025 \cdot 90}{1.225 \cdot 10} \approx 7500$ times larger than aerodynamic drag. To conclude: aerodynamic drag will be excluded from the model, as it is insignificant in comparison to the hydrodynamic drag.

2.11. Bending stiffness

Subsea power cables are not fully flexible. Bending stiffness is one of the properties of a power cable which is indicated by the cable manufacturer. Bending stiffness has been added to the model. Subsequently the difference between results including and excluding bending stiffness are assessed, to verify whether bending stiffness is significant enough to be included for the case under consideration in the current work.

Bending stiffness is a physical property which creates bending moments in the cable. Bending moment M is dependent on the magnitude of the bending stiffness EI and on the curvature. The curvature is equal to the change of orientation over length i.e. $\frac{\delta\theta}{\delta s}$. Bending moment M can be calculated using Equation 13 [Pinto, 1995]. For simplicity a linear bending stiffness is assumed in the current work while in reality cables show hysteric bending response (i.e. the EI is dependent on the curvature history) [Tan et al., 2007].

$$M = EI \cdot \frac{\delta\theta}{\delta s} \quad (13)$$

The difference in bending moment between two points on the cable creates a shear force couple at these points, which is oriented perpendicular to the longitudinal axis of the cable. Shear force S is equal to the change of bending moment over length, as shown in Equation 14 [Pinto, 1995]. Bending stiffness is accounted for by including shear force S in the EOM.

$$S = \frac{\delta M}{\delta s} = EI \cdot \frac{\delta^2\theta}{\delta s^2} \quad (14)$$

Results from two static cable configurations have been compared: one case without bending stiffness and one case with bending stiffness. Both cases model cable A (see Table 6) in 40m water and with $EA = 55.6 MN$. The maximum value of EI from the bending stiffness range given in Table 6 is used. The cable geometry and tension for both cases are shown in Figure 12 and 13, respectively.

When including bending stiffness, the tension decreases with percentages between 6 and 25%, depending on location on the cable. Tension decreases because when resistance against bending is added, the cable straightens out. When EI goes to infinity and $EI \gg EA$, the cable approaches the straight line indicated in Figure 12. The unstretched cable length in the case under consideration is 62m. When the cable's shape approaches a straight line i.e. when bending stiffness is increased, the stretched (or rather compressed) cable length is smaller than the unstretched line. Therefore, as seen in Figure 13, including bending stiffness yields a decrease of cable tension. Considering

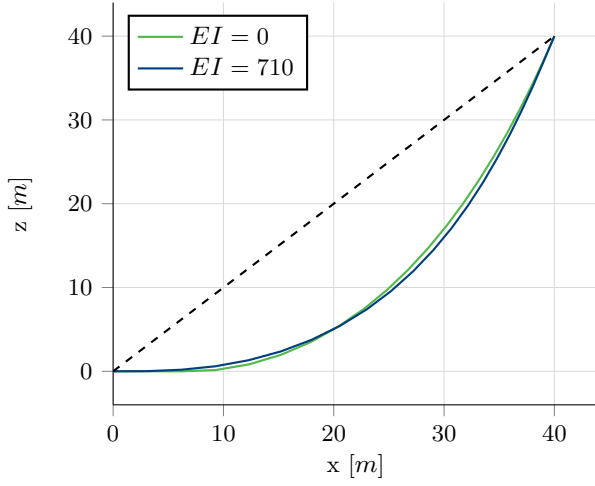


Figure 12: Static cable geometry when in- or excluding bending stiffness. The dashed straight line indicates the cable geometry when $EI \rightarrow \infty$. Bending stiffness is given in $[kNm^2]$.

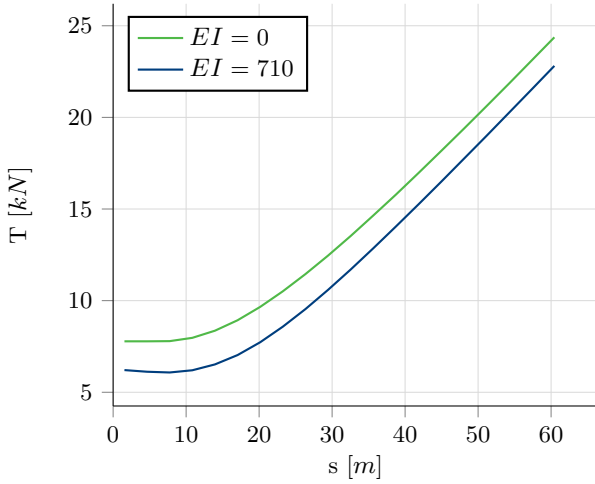


Figure 13: Static cable tension when in- or excluding bending stiffness. Bending stiffness is given in $[kNm^2]$.

the significant changes in cable tension, bending stiffness will be included in the model.

During dynamic modeling the cable without bending stiffness, spurious kinks were observed e.g. near the touch down point. Including bending stiffness prevents these kinks from occurring, which is in line with a statement made in [Pinto, 1995]: “The inclusion of the cable bending stiffness in the analysis is fundamental to guarantee continuity in slope.”

2.12. Torque moments

Similar to bending stiffness creating bending moments, torsional stiffness is a material property which creates torque moments in the cable. According to [Pinto, 1995], the main source of these moments in the dynamic analysis of subsea cables comes from the coupled axial-torsional effects associated with armoured cables. A distinction is made between cables with helical and contra-helical armour layers. In the former, torque is generated by applying tension to the cable as the armour wires are stretched. Cables with contra-helical armour are designed to have torsional balance under tensile load. Therefore, for the analysis of cables with contra-helical armour it is reasonable to neglect the axial-torsional effect and thus torque moments. Also, axial-torsional

effects are expected to only be of influence for local stability of the cable [Pinto, 2007]. As the current work focuses on global cable effects and because it is assumed that the modeled cable has a contra-helical armour, torque moments are neglected.

2.13. Structural damping

Structural damping is caused by internal friction of members inside a material. For flexible cables in water, the structural damping ratio ζ is typically ranging from 0.03 to 0.04 [DNV GL, 2017]. Following definitions from [Metrikine and Vrouwenvelder, 2016] ratio ζ is defined in Equation 15 where c and c_{cr} are damping and critical damping constants. Constant c_{cr} can be calculated using Equation 16, where stiffness k equals $\frac{EA}{l}$ for an axial structural member [Craig Jr. and Kurdila, 2006] and m_{el} is the mass of one cable element (cable elements are defined in Section 4). Mass m_{el} equals $(m \cdot l)$.

$$\zeta = \frac{c}{c_{cr}} \quad (15) \quad c_{cr} = 2\sqrt{k \cdot m_{el}} = 2\sqrt{\frac{EA}{l} \cdot m_{el}} \quad (16)$$

In order to assess whether structural damping is relevant to include in the model, the average force in the cable resulting from structural damping is analyzed. This is done using the real-time model proposed in the current work for cable A with $d = 40m$ and with the same dynamic excitation of the cable as used in Section 4.3.2. Structural damping force F_{SD} can be calculated using Equation 17 [Metrikine and Vrouwenvelder, 2016].

$$F_{SD} = c \cdot \frac{\Delta l}{\Delta t} = 2\sqrt{EA \cdot m} \cdot \frac{\Delta l}{\Delta t} \quad (17)$$

For a conservative assessment of the structural damping force, the highest ζ from the range specified in [DNV GL, 2017] is used (0.04). Force F_{SD} is dependent on change in cable length Δl , which is expected to be highest where cable tensions are highest which is at the departure point. Therefore, the rate of change of element length in the cable element adjacent to the departure point is used. The average value of F_{SD} in the mentioned cable element during the harmonic movement defined in Section 4.3.2 equals $462.6N$, which equals 2.1% of the mean tension in the respective cable element. As excluding structural damping from the model yields a model error which is smaller than the acceptable error defined in Section 2.1 in the most conservative case, structural damping is not included in the real-time model.

2.14. Equation Of Motion

Sections 2.2 to 2.13 presented physical phenomena which are included in the model. These phenomena add forces to the cable which are dependent on the cable’s position, velocity, acceleration and/or characteristics such as mass. These forces are defined in the relative subsections of Section 2. When these forces are combined into one equation, the motion of the cable can be calculated. This equation is the EOM of the physical system and is given in Equation 18, where position vector \mathbf{u} is defined in Equation 19. The included physical phenomena are (in order of appearance in Equation 18): inertia, added mass, normal hydrodynamic drag, seabed, axial stiffness, bending stiffness, buoyancy and gravity.

$$(m + m_a)\ddot{\mathbf{u}} - \frac{1}{2} \cdot \rho \cdot C_{D,n} \cdot D \cdot l \cdot V_p(\dot{\mathbf{u}})^2 - c_s \cdot \dot{\mathbf{u}} - k_s \cdot \mathbf{u} - EA \cdot \epsilon(\mathbf{u}) - EI \cdot \frac{\delta^2 \theta}{\delta s^2}(\mathbf{u}) - m_{sub} \cdot \mathbf{g} = 0 \quad (18)$$

$$\mathbf{u} = \begin{bmatrix} x \\ z \end{bmatrix} \quad (19)$$

2.15. Coordinate system

Only in-plane cable motions are considered in the current work, therefore a two-dimensional coordinate system is used. The global coordinate system is defined in Figure 14.

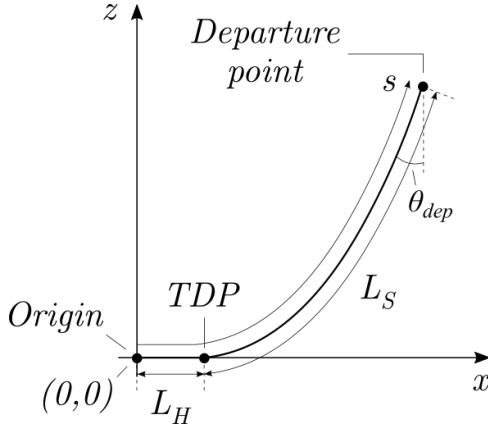


Figure 14: Global two-dimensional coordinate system. Total cable length L consists of a horizontal part which lies on the seabed (L_H) and a suspended part (L_S).

2.16. Boundary conditions

The modeled cable consists of the suspended cable plus a horizontal cable part which lies on the seabed. These parts are indicated with L_S and L_H in Figure 14, respectively. As explained in Section 2.7, the reason for including L_H in the model is to be able to calculate the dynamic location of the TDP. Therefore the length of L_H has to be larger than zero during dynamic excitation of the cable. On the other side, the length of L_H should be minimized because a longer cable means a higher computational expense. In addition, because no seabed friction is taken into account, the tension and geometry of the cable are not expected to change in cable part L_H . Hence the length of L_H should be minimized, but should always be larger than zero. This statement allows for determining the location of the boundary condition (BC) on the left-hand side of the cable.

Right of the departure point, the cable is supported by the vessel's chute (by definition), as shown in Figure 16. As the chute provides friction and a normal force to the cable, the tension in the cable decreases right of the departure point. Additionally, the geometry of the cable is secured by chute design: the chute has a larger bending radius than the cable's MBR. For these reasons, the cable tension and geometry right of the departure point are not of interest in the current work. In general the highest tension in the cable occurs just left of the departure point, and the lowest bending radius of the cable is generally found right of the TDP. Following the provided argumentation, the departure point is a reasonable location for the right-hand side BC of the cable model.

Two BCs have thus been defined: one at the origin and one at the departure point. The locations of these two BCs are fixed in the model. The boundaries are modeled as hinged ends which are fixed. The coordinates of the BCs are a model input, and these inputs can be adjusted during model runtime. For example, the departure point BC can be dynamically moved

in space to simulate vessel motions. The BCs of the model are shown in Figure 15.

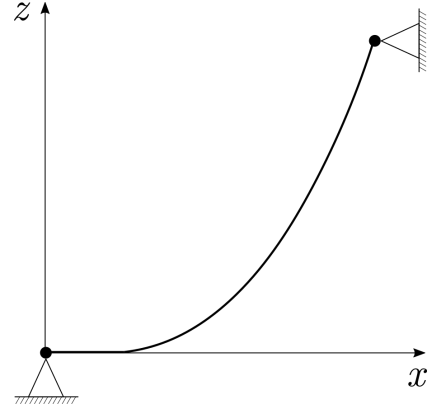


Figure 15: Boundary conditions of the cable model.

2.17. Initial condition

The initial condition (IC) of the cable consists of the cable's total length L and its geometry. Defining the IC is done in two parts. In Section 2.17.1 the horizontal cable of length L_H is defined. Subsequently the suspended cable part of length L_S is defined in Section 2.17.2. The total cable length can finally be calculated with Equation 20. The initial velocity of the cable is zero.

$$L = L_H + L_S \quad (20)$$

2.17.1. Horizontal cable

As outlined in Section 2.16, length L_H should be minimized but is required to be always larger than zero. The maximum movement of the TDP in negative x -direction is a function of cable dynamics. The cable dynamics in turn is a function of vessel motions and sea state. Therefore, an estimation of the minimum x -location of the TDP could be made based on expected vessel motions and sea state. To accelerate this estimation process, a database could be created in which TDP locations are given as function of vessel motions and sea state. The development of such a database is however out of the scope of the current work. The value for L_H used in the model is based on estimations and trial-and-error. The geometry of the horizontal cable part is defined by Equations 21 and 22, where s_H is the arc distance of the horizontal cable from the origin. The origin in these equations is the general origin of the coordinate system defined in Figure 14. The value calculated with Equation 21 is an estimate of the static position of the cable once it has settled into the seabed.

$$z_{L_H} = \frac{D}{2} - \frac{W_{element}}{k_{soil}} \quad (21)$$

$$x_{L_H}(s_H) = s_H \quad (22)$$

2.17.2. Suspended cable

The geometry of a static suspended cable in which axial and bending stiffness are neglected is taken as IC, because such a geometry follows a hyperbolic-cosine shape and can be analytically computed. Using the catenary formulas from [DNV GL, 2015], the suspended cable geometry can be calculated. Equations 23 to 25 are used, where A is a calculation constant, T_{bot} is bottom

tension (at TDP), m_{sub} is the submerged cable weight, s_S is the arc distance from the origin and x_{L_S} and z_{L_S} are the horizontal and vertical coordinate of the cable, respectively. The origin in these equations is the TDP of the cable.

$$A = \frac{T_0}{m_{sub} \cdot g} \quad (23)$$

$$z_{L_S}(s_S) = \sqrt{A^2 + s_S^2} - A \quad (24)$$

$$x_{L_S}(s_S) = A \cdot \sinh^{-1} \left(\frac{s_S}{A} \right) \quad (25)$$

To calculate A , an estimate of T_0 needs to be made. A good estimate for T_0 is the desired bottom tension during operation. To create a feasible trenching operation, T_0 should be low (in the order of several kilo Newtons) and preferably as low as possible. However T_0 should not be too close to zero, to prevent compression during dynamic excitation. For a North Sea cable lay project at $d = 40m$, typically a bottom tension of $5kN$ is desirable.

The cable is assumed to be fully submerged. Therefore, when A and the water depth are known, the suspended cable length can be calculated. This is done by using a rewritten version of Equation 24, which is given in Equation 26 where d is water depth. By substituting values between 0 and L_S into Equations 24 and 25 for s_S , the geometry of the suspended cable can be calculated.

$$L_S = \sqrt{2 \cdot A \cdot d + d^2} \quad (26)$$

2.18. Measurements as input

The thesis objective given in Section 1 states that the model should use real-time measurements as input. Measurements can be used at model start-up and during model runtime, as outlined in Section 2.18.1 and 2.18.2.

2.18.1. Measurements at model start-up

Section 2.17.2 specifies that an estimate for bottom tension T_0 is required for calculating the modeled cable length and thus initial condition of the model. When departure angle θ_{dep} , water depth d and submerged cable mass m_{sub} are known, bottom tension T_0 can be calculated using Equation 27 from [DNV GL, 2015].

$$T_0 = \frac{m_{sub} \cdot d \cdot \sin(\theta_{dep})}{1 - \sin(\theta_{dep})} \quad (27)$$

Equation 27 neglects bending and axial stiffness. Neglecting bending stiffness is expected to cause a minor difference in geometry (shown for $EI = 710kNm^2$ in Figure 12) and neglecting axial stiffness is expected to cause a geometry deviation from the numerical equilibrium cable geometry of $0.18D$ for cable A and $d = 40m$, as outlined in Section 5.1. Both of the mentioned deviations in cable geometry of the initial condition are marginal and quickly disappear after model start-up (within 10s).

Departure angle θ_{dep} can be measured by a Departure Angle Measurement System (DAMS), which is typically present on cable laying vessels. When the model is initialized the DAMS provides the current θ_{dep} , the model estimates T_0 using Equation 27 and subsequently computes the initial condition.

The vessel's position and orientation in space are measured by its Motion Reference Unit (MRU). In combination with a bathymetry map (obtained from survey analysis), the position of the two BCs defined in Section 2.16 can be determined. Knowing

the position and orientation of the cable lay vessel (and thus the chute) in space is not enough for determining the exact location of the departure point, though. As shown in Figure 16 the departure point position is also dependent on θ_{dep} .

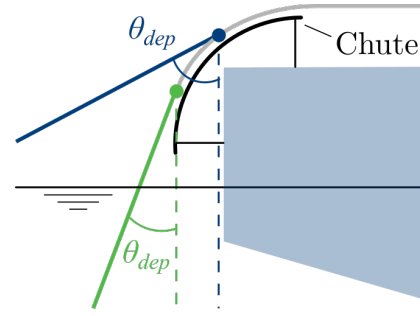


Figure 16: *Departure point location is dependent on chute location and θ_{dep} .*

Additional to using the DAMS measurement for estimating T_0 , it can be used for determining the exact location of the departure point on the chute. It is required to know the location of the departure point as this is one of the model's BCs.

2.18.2. Measurements during model runtime

During cable lay, the location of the departure point moves in space due to vessel motions and changes in departure angle. The vessel MRU continuously measures the vessel motions and the DAMS continuously measures θ_{dep} . Combining these two measurements, the departure point location can be adjusted during operation. For a seabed which is not flat, the seabed profile (obtained from survey analysis) can be used to determine the varying location of the seabed BC.

Once the model has started, the modeled cable has a certain length and mean layback length. During cable lay operations, the layback length is occasionally changed. This is done by temporarily paying out the cable with a higher or lower speed than the vessel velocity. When the layback length is changed, the model should be re-started with a new initial condition. The change in layback length can automatically be detected by the model by comparing the mean θ_{dep} calculated in the model and the mean θ_{dep} measured by the DAMS. In case these two quantities are off for a set period of time, the model should be re-started with a new initial condition. The procedure described at Section 2.18.1 is then initiated again.

3. Real-time modeling

The explanation in the current section is supported by Figure 17, which contains some key concepts. These concepts are outlined in Sections 3.1-3.3. The consequences of modeling in real-time are described in Section 3.4. A comparison between fixed and variable timesteps is made in Section 3.5.

3.1. Data input

Figure 17 shows an arbitrary continuous data stream, which represents for example the measurement of the departure point position. Even though in practise measurement devices have a specific data output rate, the model will interpolate between the provided data points in order to have a continuous input data stream available.

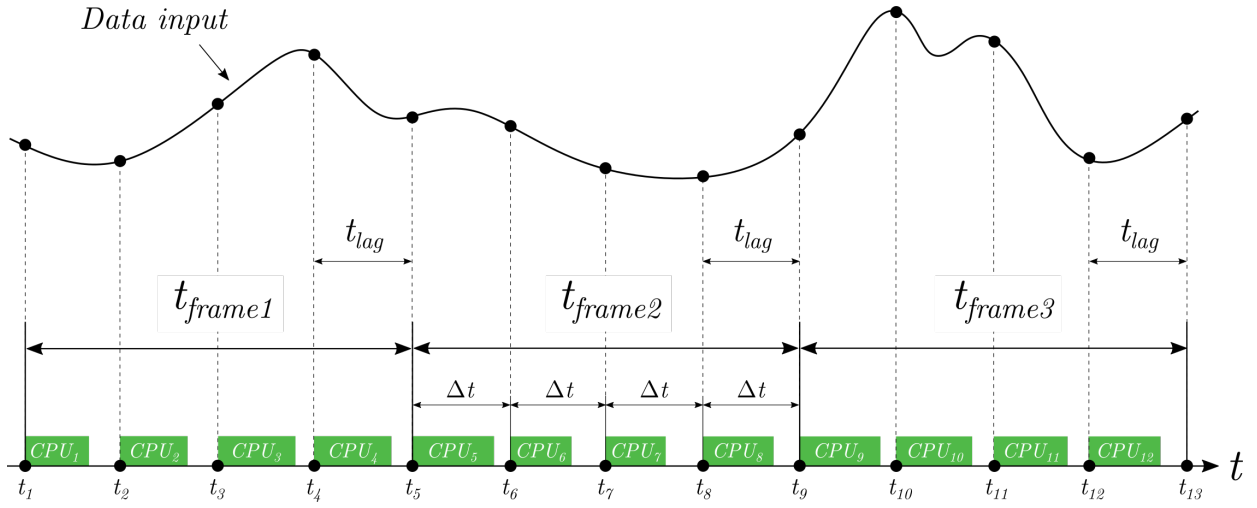


Figure 17: Illustration of real-time simulation with a fixed timestep. Green blocks indicate the time during which the next cable state is calculated.

3.2. Model timestep

Suppose that the model timestep Δt shown in Figure 17 is fixed, equals $\frac{1}{120}s$ and satisfies this condition. Hence in this case the rate at which the model re-calculates the cable's state is $120Hz$.

At the start of a new model timestep at t_i , input data is collected from the data stream at t_i . Instantly afterwards, the numerical model computes the cable's state based on the new input. The time required for computing the new state is indicated with the green block named CPU_i in Figure 17.

3.3. Visualization with framerate

As specified by the thesis objective, the proposed AR simulation has to be updated in real-time. To ensure a smooth AR rendering, the rate of refreshing the visualization (i.e. the *framerate*) should be at least $30Hz$ [Ref]. However, the framerate doesn't have to be higher than $60Hz$ as a framerate higher than $60Hz$ will not increase the smoothness of the visualization. Suppose that the framerate used in Figure 17 is $30Hz$ and hence $t_{frame} = \frac{1}{30}s$. The ratio between frame duration and model timestep is introduced in Equation 28. For the example case shown in Figure 17, $\eta = \frac{120}{30} = 4$.

$$\eta = \frac{t_{frame}}{\Delta t} \quad (28)$$

Each frame visualizes the cable state calculated in the most recent past timestep: this is a snapshot of the discrete modeled cable state. Using the parameters defined in Figure 17: frame 2 shows the cable state which has been calculated between t_4 and t_5 . Frame 2 starts visualizing the cable state which has been calculated based on data inputs from t_4 at t_5 . Therefore the visualization of the physical cable system is not exactly real-time, but is lagging behind reality with t_{lag} . As will be shown in Section 4.4, the required timestep for modeling a cable with a realistic axial stiffness and a reasonable amount of elements is in the order of several milliseconds. As t_{lag} is equal to the duration of the most recent past timestep, t_{lag} also will be in the order of several milliseconds. Hence the time shift from data input to visualization is negligible. However the following applies: In order to achieve a real-time simulation, duration t_{gap} should be minimized. A smaller t_{lag} means a simulation which runs closer to real time.

3.4. Consequences of modeling in real-time

The most important consequence of modeling in real-time is quantitatively given by Equation 29, where $t_{CPU,i}$ is the required time to calculate the new cable state based on the data input at t_i and η is defined by Equation 28. Duration $t_{CPU,i}$ is indicated by the green blocks in Figure 17. This consequence is explained qualitatively below.

$$\sum_{i=1}^{\eta} t_{CPU,i} \leq \eta \cdot \Delta t \quad (29)$$

The time required to calculate the cable state η times should be smaller than or equal to t_{frame} . For example, the time to compute the cable state at t_1, t_2, t_3 and t_4 (visualized by the green blocks during t_{frame1} in Figure 17) should be smaller than or equal to t_{frame1} . If this is *not* the case, the frame shown during t_{frame1} cannot visualize the cable state computed in CPU_4 , because the CPU_4 calculation would still be running. Suppose that block CPU_3 is already completed: then the cable state computed in CPU_3 becomes the most recent completed calculated cable state and t_{frame2} will visualize the cable state from CPU_3 . This increases t_{lag} for t_{frame2} . If the duration of green blocks CPU_5 to CPU_8 is longer than t_{frame2} , t_{lag} increases again. Therefore if Equation 29 is not satisfied, t_{lag} will keep on increasing with a *snowball-effect*: moving the simulation further and further away from real time. To put this into perspective: for non real-time modeling, the time taken to compute the new cable state (CPU_i) doesn't have consequences except for having to wait longer for results.

Increasing N or decreasing Δt both increase the computational expense of the model. Because of the condition given in Equation 28 and the fact that a computer has a certain available computational power, there will be a limit on the computational expense of the model for simulating in real-time. This means there also is a limit on the amount of elements and the model timestep which can be modeled in real-time, as reflected by Table 3.

3.5. Fixed versus variable timestep

In case of real-time modeling, the time to calculate the next state should be smaller than or equal to the timestep (multiplied with η), as given by Equation 29. For this explanation, a fixed computational time for each timestep is assumed and is indicated

by t_c . Figure 18 visualizes this case with a variable and fixed timestep.

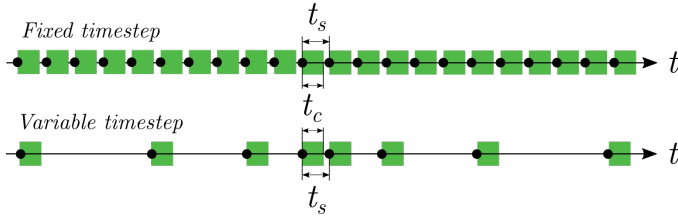


Figure 18: Fixed versus variable timesteps. Green blocks indicate the time during which the next cable state is calculated.

The smallest timestep used (t_s) has to be larger than the fixed computational time t_c , both in the case of a variable and fixed timestep. The advantage of a variable timestep would be a reduction in computational expense for timesteps larger than t_s . The computer could idle more when it has finished processing after t_c , before the new timestep would start.

As the computer is able to compute the new cable state within t_s , the model timestep could also be always equal to t_s (resulting in a fixed timestep) instead of only sometimes (which is the case using a variable timestep). The disadvantage of this, is that the computer is stressed more. A variable timestep hence is more beneficial from a computational perspective. However, a variable timestep is significantly more challenging to program than a fixed timestep. Hence from a programming point of view, the fixed timestep is more beneficial. As the sole envisioned consequence of using a fixed timestep while modeling in real-time is a higher strain of the computer's processor, and because a fixed timestep is less challenging to program, a fixed timestep is used in the model presented in the current work.

4. Numerical solution

In order to obtain a numerical solution to the governing equations given in Section 2, the physical system is discretized in Section 4.1. The advancement of the discretized system in time is found using the numerical method outlined in Section 4.2. Static and dynamic errors induced by discretization of the physical system are reported in Section 4.3. Model stability is analyzed in Section 4.4. Subsequently the performance optimization of the model is presented in Section 4.5. Finally the consequences of modeling a lower axial stiffness than the axial stiffness of the physical cable are given in Section 4.6.

4.1. Discretization

Due to the high non-linearity of the tension and geometry of the cable, the continuous cable will be discretized in order to model it. The cable is discretized using a lumped mass method, as done by [Boom, 1985] for modeling the behaviour of a continuous mooring line. The cable is modeled as a group of lumped masses (*nodes*) which are connected by massless springs (*elements*). Figure 19 shows how the cable is discretized for an example case with $N = 6$. Key parameters for the discrete cable model are: horizontal distance between two nodes Δx , vertical distance between two nodes Δz , element orientation θ , unstretched element length l_0 and stretched element length l_s . These parameters are calculated using Equations 30-34.

$$\Delta x = n_{j,x} - n_{i,x} \quad (30) \quad \Delta z = n_{j,z} - n_{i,z} \quad (31)$$

$$\theta = \text{atan} \left(\frac{\Delta z}{\Delta x} \right) \quad (32) \quad l_0 = \frac{L}{N} \quad (33)$$

$$l_s = \sqrt{\Delta x^2 + \Delta z^2} \quad (34)$$

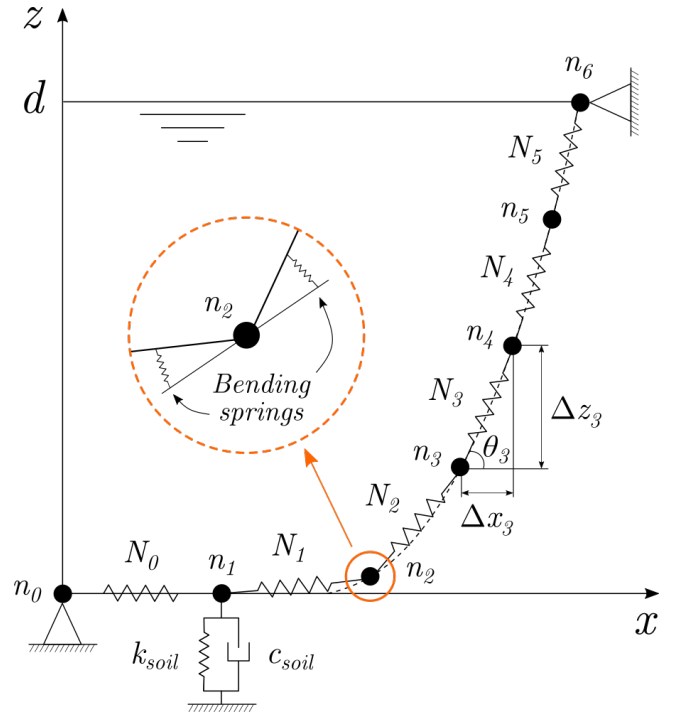


Figure 19: Discretization of the cable, for $N = 6$. The figure zooms into node 2 to show the bending springs.

The EOM presented in Section 2.14 is applied to each node, yielding two discrete EOMs per node: one for motions in x -direction and another for motions in z -direction. Therefore, a node has one EOM per Degree Of Freedom (DOF). The discrete EOMs for x and z -direction are given in Equation 35 and 36 for node i , and are valid for non-end nodes only. The components of Equation 35 and 36 are outlined in Sections 4.1.1-4.1.5.

$$(m + m_a)\ddot{x}_i = F_{a,x,i} + F_{d,x,i} + S_{x,i} \quad (35)$$

$$(m + m_a)\ddot{z}_i = F_{a,z,i} + F_{d,z,i} + S_{z,i} - F_g + F_{s,i} \quad (36)$$

4.1.1. Discrete axial force

Axial force is a result from cable strain in longitudinal direction, i.e. (in the discrete model) from elongation of the spring between two nodes. The derivation of the axial force in x -direction for the element right of node i is given in Equations 37-39, where Figure 20 serves as a guide for definition of parameters and spring stiffness $k = \frac{EA}{l_0}$. The axial force in the element left of node i and the z -component of the axial force can be derived likewise.

$$F_{a,x,i} = F_{a,r_x} - F_{a,l_x} \quad (37)$$

$$F_{a,r} = k \cdot (l_{ij} - l_0) = \frac{EA}{l_0} \cdot (l_{ij} - l_0) \quad (38)$$

$$F_{a,r_x} = \frac{EA}{l_0} \cdot (l_{ij} - l_0) \cdot \frac{\Delta x_{ij}}{l_{ij}} \quad (39)$$

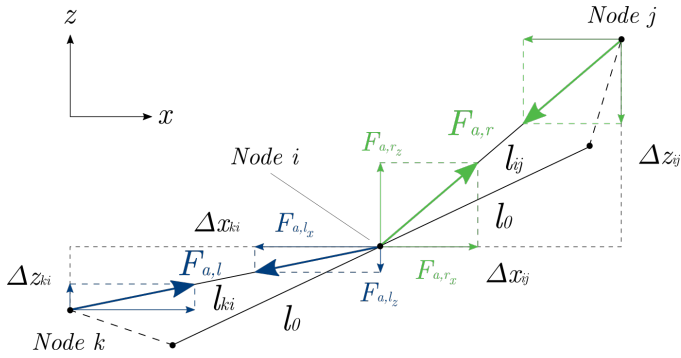


Figure 20: Force diagram of stretched elements around node i .

4.1.2. Discrete hydrodynamic drag force

The hydrodynamic drag force on each element is calculated using Equation 3. Subsequently this force is decomposed into a x and z -component with Equation 40 and 41, respectively. Each node takes half of the hydrodynamic drag force from its right neighboring element (ij) and half of the hydrodynamic drag force from its left neighboring element (ki), as shown for the x -component by Equation 42.

$$F_{d,ij,x} = F_{d,ij} \cdot \cos(\theta) \quad (40)$$

$$F_{d,ij,z} = F_{d,ij} \cdot \sin(\theta) \quad (41)$$

$$F_{d,x,i} = \frac{1}{2}(F_{d,ij,x} + F_{d,ki,x}) \quad (42)$$

4.1.3. Discrete shear force

As indicated in Section 2.11, the difference in bending moment between two points on the cable creates a shear force couple at these points, which is oriented perpendicular to the longitudinal axis of the cable. In the discretized model, the shear force couple is applied at the nodes of an element. Figure 21 visualizes this and also supports the remainder of the current section. In order to calculate the magnitude and direction of the shear forces, first the bending moments per cable element are determined using the discrete version of Equation 13. The discrete bending moment of element i is calculated with Equation 43, where ω is the angle that the element makes with the vertical. Angle ω is counted in counterclockwise direction and is calculated using an *atan2* function in order to be able to compute the cable orientation in 360 degrees, which is not possible with the regular *atan* function.

$$M_i = EI \cdot \left(\frac{\Delta\omega}{\Delta s} \right)_i = EI \cdot \left(\frac{\omega_{i+1} - \omega_{i-1}}{2 \cdot l_0} \right) \quad (43)$$

End elements have no neighboring element on one side, which yields one unknown in Equation 43: ω_{i+1} for the right and ω_{i-1} for the left end element. Therefore, a fictitious neighboring element is used which is assumed to have the same orientation as element i . For the left end element, this is a reasonable assumption because the laid cable left of the origin has an approximately equal orientation to the cable right of the origin point. The validity of this assumption is depending on l_0 for the right end element: a smaller l_0 means a more accurate approximation. The bending moment of e.g. the left end element is calculated using Equation 44.

$$M_0 = EI \cdot \left(\frac{\omega_1 - \omega_0}{2 \cdot l_0} \right) \quad (44)$$

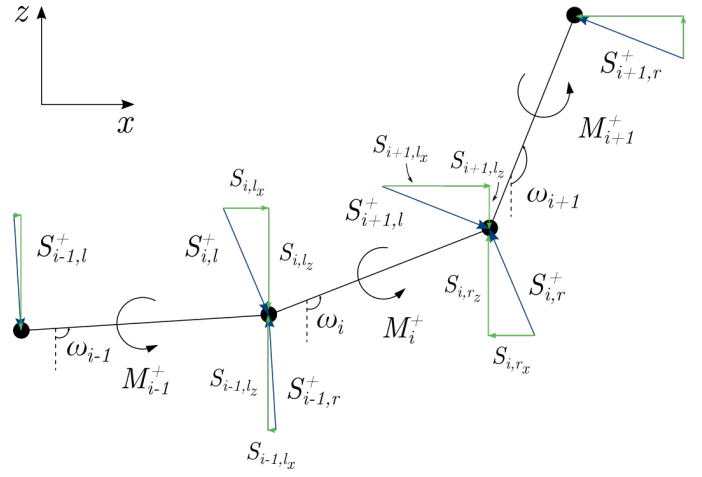


Figure 21: Discrete shear forces on the nodes as result of bending moments in the elements. Blue arrows indicate shear force couples. Green arrows represent the shear force x and z -components.

The discrete variant of Equation 14 computes the magnitude and direction of the shear force couple on element i , and is given in Equation 45 for non-end elements. The shear force for the left and right end elements is calculated using Equation 46 and 47, respectively.

$$S_i = \frac{\Delta M}{\Delta s} = \frac{M_{i+1} - M_{i-1}}{2 \cdot l_s} \quad (45)$$

$$S_0 = \frac{M_1 - M_0}{l_s} \quad (46) \quad S_{N-1} = \frac{M_{N-1} - M_{N-2}}{l_s} \quad (47)$$

When the magnitude and direction of the shear force couples have been calculated for each element, the individual shear forces which are applied to the left and right node of the element are decomposed into an x and z -element. This is done with Equations 48-51. Finally the resultant shear force per node is calculated for x and z DOFs using Equation 52 and 53.

$$S_{i,l_x} = -S_i \cdot \sin(\omega_i) \quad (48) \quad S_{i,r_x} = S_i \cdot \sin(\omega_i) \quad (49)$$

$$S_{i,l_z} = -S_i \cdot \cos(\omega_i) \quad (50) \quad S_{i,r_z} = S_i \cdot \cos(\omega_i) \quad (51)$$

$$S_{x,i} = S_{i,l_x} + S_{i-1,l_x} \quad (52) \quad S_{z,i} = S_{i,l_z} + S_{i-1,l_z} \quad (53)$$

4.1.4. Discrete weight force

Each node is lumped with half the mass of its left neighboring element and half the mass of its right neighboring element. As each element has an equal length, the weight on each node is equal and is calculated with Equation 54.

$$F_g = m_{sub} \cdot l_0 \cdot g \quad (54)$$

4.1.5. Discrete soil force

The lumped point mass which represents a cable element of length l_0 has no diameter, but the physical cable has a diameter. The soil reaction force given in Equation 7 should be applied when the cable touches down on the seabed. When the z -coordinate of a descending node becomes zero, the discretized cable touches down. However a descending physical cable would have touched down earlier, because of its diameter. This explanation is supported by Figure 22. For this reason the soil force

given in Equation 7 is now applied for $z < \frac{D}{2}$. Additionally, the soil damping force is only applied in case the cable is moving into the soil i.e. when $\dot{z} < 0$. These two adjustments to the conditions of the soil force yield Equation 55.

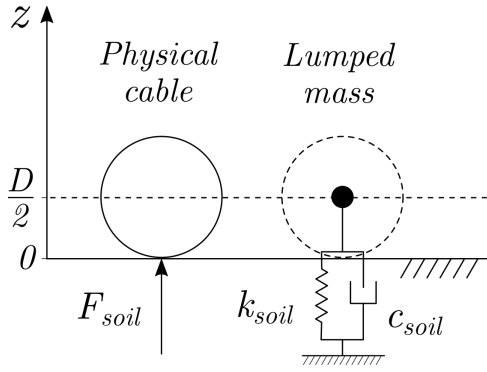


Figure 22: Cross-section of a cable touching the seabed.

$$F_{s,i} = \begin{cases} -\sqrt{4mk_s} \cdot \dot{z} + k_s \cdot (\frac{D}{2} - z), & z < \frac{D}{2} \ \& \ \dot{z} < 0 \\ k_s \cdot (\frac{D}{2} - z), & z < \frac{D}{2} \ \& \ \dot{z} > 0 \\ 0, & \text{else} \end{cases} \quad (55)$$

4.2. Numerical method

The discretized EOMs presented in Section 4.1 are solved using the numerical method described in the current section. In line with the numerical implementation used for the dynamic cable model made by [Pinto, 2007], a time domain approach is used because the presented EOMs are highly non-linear. Section 4.2.1 outlines the made comparison between implicit and explicit methods. The selected numerical method is given in Section 4.2.2.

4.2.1. Implicit versus explicit

Two general methods for numerically solving dynamic problems exist: implicit and explicit. Explicit methods determine the system state at the new time step t_{n+1} using known values at the current time step t_n . Implicit methods determine the system state at t_{n+1} using unknown values at t_{n+1} [Ferziger and Peric, 2002]. Both methods have several advantages and disadvantages. Implicit methods are unconditionally stable and permit large time steps, but computational expense per time step is high. Explicit methods are less computationally expensive per time step but require small time steps for numerical stability. The most efficient method is different for each problem [Hughes and Liu, 1978]. Hence for determining the most efficient method for the problem of modeling cable dynamics, both methods should be applied and analyzed.

The cable model proposed in the current work has been developed from scratch in the programming language C#. The choice for C# is clarified in Section 6.1. In order to numerically solve for the unknowns \ddot{x}_i and \ddot{z}_i given in Equations 35 and 36, an ordinary differential equation (ODE) solver has to be used. Basic mathematical operations can be performed using a built-in class in C#, but more advanced algorithms are lacking by default. However, the *Math.NET Numerics library* can be used to enable more advanced numerical computations like ODE solving in C#. Implicit ODE solvers are not available in the Math.NET Numerics library, although explicit ODE solvers are. This yields that in order to use an implicit method in the proposed real-time model, an implicit ODE solver has to be

constructed from scratch. The wide scope and fixed period of time set for the current research therefore resulted in the choice for an explicit method.

4.2.2. Fourth-order Runge-Kutta

Position vector \mathbf{u} from Equation 19 and its time derivative together define state vector \mathbf{q} , which is given for one node at t_n in Equation 56. State vector \mathbf{q} is of size $2 \cdot \text{DOF}$. An ODE solver is used to find \mathbf{q} at t_{n+1} . Equation 57 shows a Forward Euler (FE) ODE solver which has a local truncation error with an order of magnitude of Δt^2 .

$$\mathbf{q}_n = \begin{bmatrix} x_n \\ z_n \\ \dot{x}_n \\ \dot{z}_n \end{bmatrix} \quad (56)$$

$$\mathbf{q}_{n+1} = \begin{bmatrix} x_n + (\dot{x}_n \cdot \Delta t) \\ z_n + (\dot{z}_n \cdot \Delta t) \\ \dot{x}_n + (\ddot{x}_n \cdot \Delta t) \\ \dot{z}_n + (\ddot{z}_n \cdot \Delta t) \end{bmatrix} = \mathbf{q}_n + \dot{\mathbf{q}}_n \Delta t + O(\Delta t^2) \quad (57)$$

The current work uses an explicit fourth-order Runge-Kutta (RK) solver, because this ODE solver provides a higher accuracy than the FE solver shown in Equation 57. The used RK solver is an available solver in the C# Math.NET Numerics library [Ruegg et al., 2017]. The RK solver finds the system state at t_{n+1} using a similar principle as Equation 57 but with a smaller truncation error, as shown in Equation 58 [Keijdener and Jarquin-Laguna, 2017]. The difference with the FE solver is that the RK solver makes four preliminary estimates of \mathbf{q}_{n+1} before definitively computing \mathbf{q}_{n+1} . The local truncation error of the fourth-order RK solver is in the order of Δt^5 .

$$\mathbf{q}_{n+1} = f_{RK4}(\mathbf{q}_n) + O(\Delta t^5) \quad (58)$$

As is the case for Equation 57, the only unknown in Equation 58 is the time derivative of the state vector $\dot{\mathbf{q}}_n$. Vector $\dot{\mathbf{q}}_n$ is defined in Equation 59. Velocities \dot{x}_n and \dot{z}_n are known from \mathbf{q}_n . Accelerations \ddot{x}_n and \ddot{z}_n are calculated using Equations 35 and 36.

$$\dot{\mathbf{q}}_n = \begin{bmatrix} \dot{x}_n \\ \dot{z}_n \\ \ddot{x}_n \\ \ddot{z}_n \end{bmatrix} \quad (59)$$

4.3. Discretization error

The discretization error is analyzed both for static and dynamic results in Section 4.3.1 and 4.3.2, respectively. Errors are classified as acceptable or not based on the definition of acceptable errors given in Section 2.1.

4.3.1. Static discretization error

To correctly assess the discretization error in a static state, static cases with different element lengths are compared. As shown in Section 4.4, the workable range of element lengths in order to model a cable in real-time with an axial stiffness between $1000MN$ and $22MN$ is from $6.2m$ to $1.55m$, respectively.

In order to precisely determine the static discretization error of the real-time model, results from a static case with a very small element length (in the order of a few centimeters) are required. This static case with a very small l_0 will be referred

to as the *static base case*. The static base case is assumed to have a negligible discretization error itself, due its very small l_0 . The results from static cases with the mentioned workable range of element lengths, produced by the real-time model, can then be compared to results from the static base case in order to determine the discretization error.

As shown in Figure 36, the model timestep must be extremely small to model a cable with a realistic axial stiffness and an element length of a couple of centimeters. More specifically, typical values for axial stiffness are minimally $17.5MN$ and $400MN$ for infield and export subsea cables respectively, as given in Appendix A.2.2. An estimation of the required timestep to prevent instability with $EA = 50MN$ and $l_0 = 0.03m$ is made based on Equation 76. The inverse of the required timestep $\frac{1}{\Delta t}$ should be at least $23000Hz$. As shown by Table 2, the computer on which the real-time model was made is extremely far from being able to compute the cable state with $23000Hz$ with $l_0 = 0.03m$. Therefore an alternative model for finding results for the static base case is proposed.

The proposed alternative model is a numerical model capable of finding a static cable configuration using a Finite Difference Method (FDM). The alternative model is called the *FDM model*. The FDM model includes the same physics relevant in stationary cases as the real-time model, except bending stiffness. The included physics are hence: gravity, buoyancy, axial stiffness, hydrodynamic drag and seabed. The advantages of the FDM model are: it can calculate a very accurate stationary cable configuration within an acceptable amount of seconds and it can do this for very high values of EA . The advantage of the FDM model over an analytical (catenary shape) solution is that the FDM model is capable of modeling a seabed and a constant current. Mainly the capability to model the seabed is important, as this allows for determining the discretization error of the TDP.

The FDM model is capable of determining stiffness matrix \mathbf{K} and force vector \mathbf{F} for the discretized cable. Matrix \mathbf{K} is found by determining the slope of \mathbf{F} w.r.t. state vector \mathbf{u} using finite differences. The determination of $\frac{\delta \mathbf{F}}{\delta \mathbf{u}}$ is conceptually shown in Figure 23 and Equation 60.

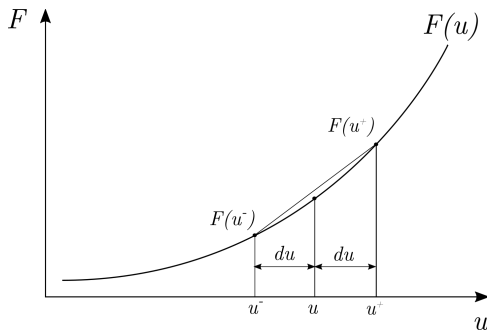


Figure 23: The FDM model finds the slope of \mathbf{F} w.r.t. \mathbf{u} using finite differences.

$$\frac{\delta \mathbf{F}}{\delta \mathbf{u}} \approx \frac{\mathbf{F}(\mathbf{u} + d\mathbf{u}) - \mathbf{F}(\mathbf{u} - d\mathbf{u})}{2d\mathbf{u}} = \frac{\mathbf{F}(\mathbf{u}^+) - \mathbf{F}(\mathbf{u}^-)}{2d\mathbf{u}} \quad (60)$$

Vector \mathbf{F} is calculated based on the equations provided in Section 2. Through iterations the FDM model converges towards a stationary cable configuration by solving Equation 61 until the condition given in Equation 62 is satisfied. The convergence condition is set to an extremely small difference between the last two iterations in order to determine a cable configuration with an extremely high accuracy to serve as the static base case.

$$\mathbf{u} = \mathbf{K} \setminus \mathbf{F} \quad (61)$$

$$\max(\mathbf{u}_{new} - \mathbf{u}_{old})^2 < 10^{-14} \quad (62)$$

The FDM model has been verified to give the same static results as the real-time model. This verification has been done with cable A from Table 6, with $EA = 22MN$ and $EI = 0Nm^2$, $L = 62m$, $d = 40m$, $k_{soil} = 100 \frac{kN}{m}$, $N = 40$ and $l_0 = 1.55m$. The resulting difference in geometry between the FDM model and the real-time model is less than $0.3mm$ for all nodes. The tension difference between the results from the two models is less than $0.5N$ for all elements. These minor differences are expected to be caused by the difference between the defined convergence condition in both models. The real-time model is deemed to be stationary when the maximum absolute node velocity is smaller than $10e^{-4}m/s$, while the FDM model is taken as converged when Equation 62 is satisfied.

The results from the static base case found by the FDM model will be compared to the results from the real-time model. For a fair comparison the modeled case should be equal in both models, which yields that the value of EA should be equal in all cases. The value of EA which can be modeled in the real-time model is limited by available computational power. As shown in Table 3, the smallest element length for which still a realistic axial stiffness can be modeled is $1.55m$. The maximum axial stiffness which can be modeled with $l_0 = 1.55m$ in the real-time model is $22MN$. Therefore EA is set to $22MN$ for all cases used in the current discretization error analysis. The cases run in order to find the static discretization error are summarized in Table 1.

Table 1: Cases run to find the static discretization error. All cases model: cable A (Table 6), $EA = 22MN$, $EI = 0Nm^2$, $L = 62m$, $d = 40m$ and $k_{soil} = 100 \frac{kN}{m}$. RT and FDM indicate the real-time and FDM model.

Model	RT	RT	RT	RT	FDM
N	10	20	30	40	1000
l_0 [m]	6.20	3.10	2.07	1.55	0.062

The dimensionless discretization error for x -coordinates, z -coordinates and element tension are denoted by ϵ_{x_s} , ϵ_{z_s} and ϵ_{T_s} respectively. The errors are calculated using Equations 63-65 where D is the cable diameter. The coordinates from the static base case are taken by linearly interpolating between the coordinates of the two nodes surrounding the node from the real-time model and then finding the static base case coordinate exactly at the coordinate from the real-time model coordinate. The tension values from the static base case are taken as the tension of the element at the same s location as the s location in the real-time model results. Dimensionless discretization errors ϵ_{x_s} , ϵ_{z_s} and ϵ_{T_s} have been evaluated for the real-time cases given in Table 1 and are shown in Figures 24-26.

$$\epsilon_{x,s} = \frac{|x_s - x_{s,N1000}|}{D} \quad (63) \quad \epsilon_{z,s} = \frac{|z_s - z_{s,N1000}|}{D} \quad (64)$$

$$\epsilon_{T,s} = \frac{|T_s - T_{s,N1000}|}{T_{s,N1000}} \cdot 100\% \quad (65)$$

As shown by Figures 24-26, the acceptable error gets exceeded by the z -coordinate error only, for $N \leq 10$. Hence in order to limit the static discretization error to the acceptable error, a discretization refinement of $3.10m$ or smaller should be used.

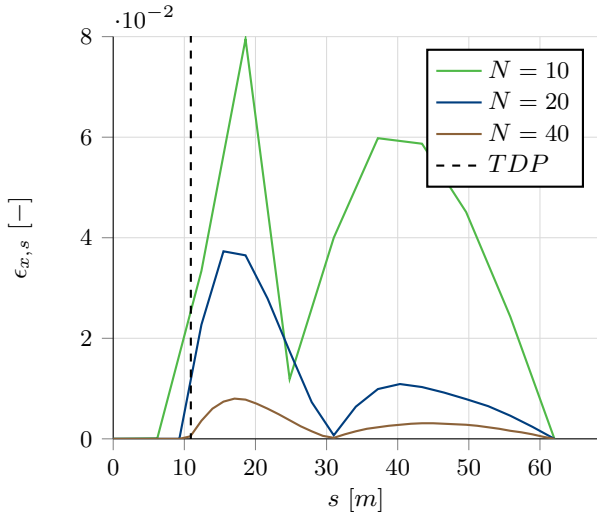


Figure 24: Static $\epsilon_{x,s}$ for various N . All errors shown are acceptable.

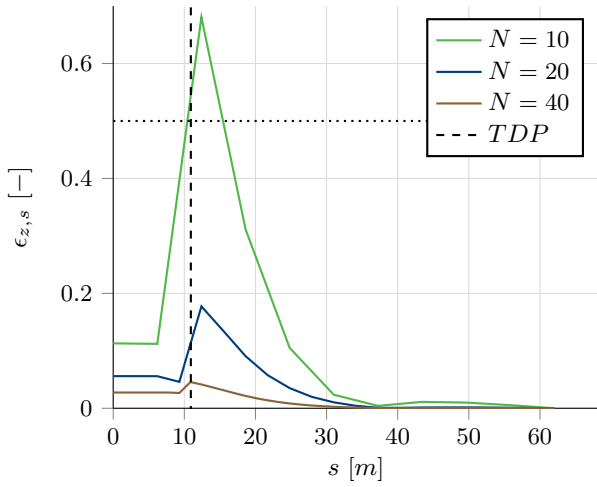


Figure 25: Static $\epsilon_{z,s}$ for various N . The acceptable error limit is indicated with the dotted horizontal line.

4.3.2. Dynamic discretization error

The discretization error is analyzed for dynamic cases as well. To this end, the real-time model cases from Table 1 have been verified with a dynamic case with many elements. For the latter, *OrcaFlex* has been used due to the limitations of l_0 and EA in the real-time model (as shown in Section 4.4). The dynamic case modeled in *OrcaFlex* has equal properties to the real-time model cases, but $N = 620$ i.e. $l_0 = 0.1m$. In all dynamic cases, bending stiffness has been included with $EI = 300Nm^2$. The cable is excited dynamically by a harmonic movement in z -direction of the departure point. This harmonic displacement is described by Equation 66, where $A_{displ} = 0.5m$ and $\omega_{displ} = 1 \frac{rad}{s}$ yielding $T_{displ} = \frac{2\pi}{\omega_{displ}} = 6.283s$.

$$z_{DP} = A_{displ} \cdot \sin(\omega_{displ} \cdot t) + z_{DP,t0} \quad (66)$$

The dimensionless dynamic discretization error will be calculated by finding the difference between the minimum, mean and maximum tension value found at a certain s location during a simulation of duration t_{sim} . Consequently a tension range graph has been made for all mentioned dynamic cases, which maps the minimum, mean and maximum tension along the full cable length. The range graphs were constructed by exciting the cable dynamically with the motion described in Equation 66

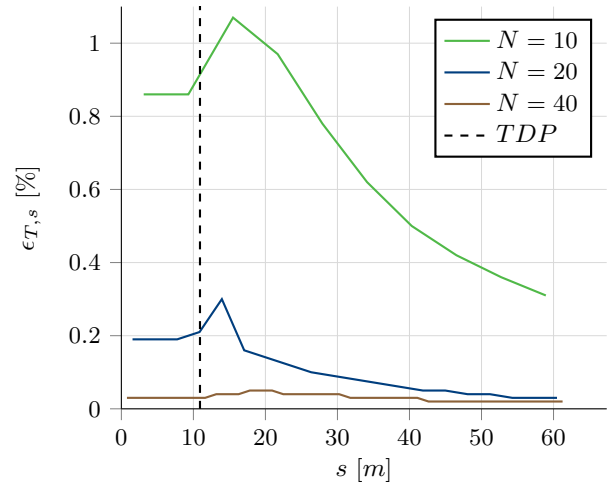


Figure 26: Static $\epsilon_{T,s}$ for various N . All errors shown are acceptable.

for a duration of 60s. As the motion of the cable converges during time (as a harmonic and constant motion defines the dynamics), only the last part of cable oscillations has been used for the range graphs. This duration t_{sim} has been taken to be a bit longer than T_{displ} ; $t_{sim} = 7s$. The resulting tension range graphs for 10, 40 and 620 elements are put together in Figure 27.

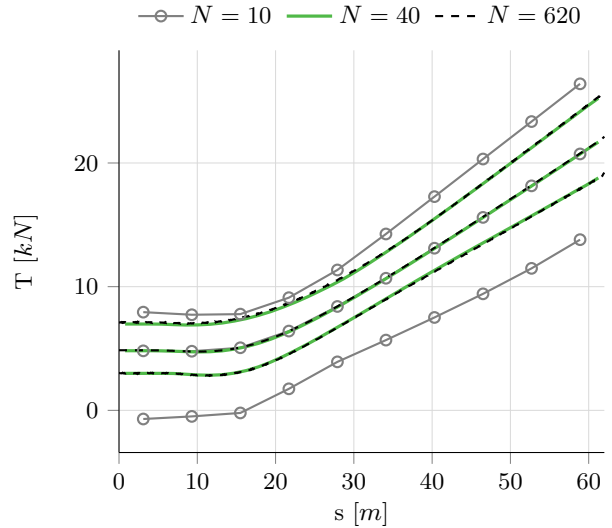


Figure 27: Tension range graph showing the minimum (bottom lines), mean (middle lines) and maximum tension (top lines) along the cable length from $t = 53s$ to $t = 60s$.

Subsequently the differences between minimum, mean and maximum tensions found at specific s -locations have been compared using Equations 67-69 where dimensionless dynamic discretization error for minimum, mean and maximum tension is denoted by $\epsilon_{Tmin,s}$, $\epsilon_{Tmean,s}$ and $\epsilon_{Tmax,s}$. Errors $\epsilon_{Tmin,s}$ and $\epsilon_{Tmax,s}$ are visualized in Figures 28 and 29. Error $\epsilon_{Tmean,s}$ is not visualized because the maximum error found in all real-time cases is 1.16%, which is deemed acceptable.

$$\epsilon_{Tmin,s} = \frac{|T_{min,s} - T_{min,s,N620}|}{T_{min,s,N620}} \cdot 100\% \quad (67)$$

$$\epsilon_{Tmean,s} = \frac{|T_{mean,s} - T_{mean,s,N620}|}{T_{mean,s,N620}} \cdot 100\% \quad (68)$$

$$\epsilon_{T_{max,s}} = \frac{|T_{max,s} - T_{max,s,N620}|}{T_{max,s,N620}} \cdot 100\% \quad (69)$$

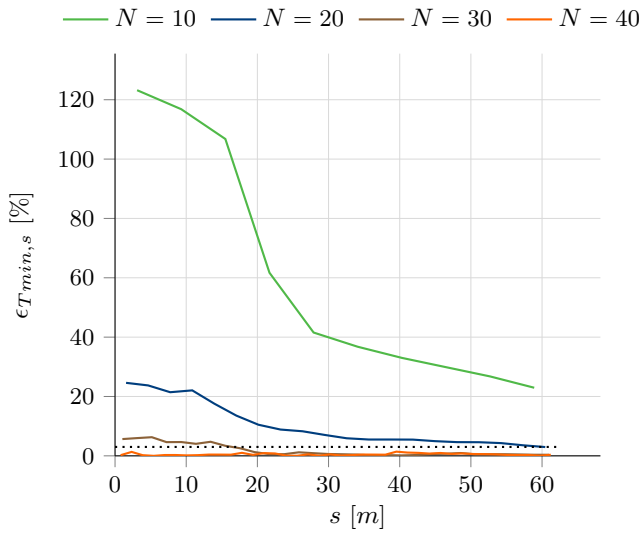


Figure 28: Dynamic error $\epsilon_{T_{min,s}}$ for various N . The acceptable error limit is indicated with the dotted horizontal line.

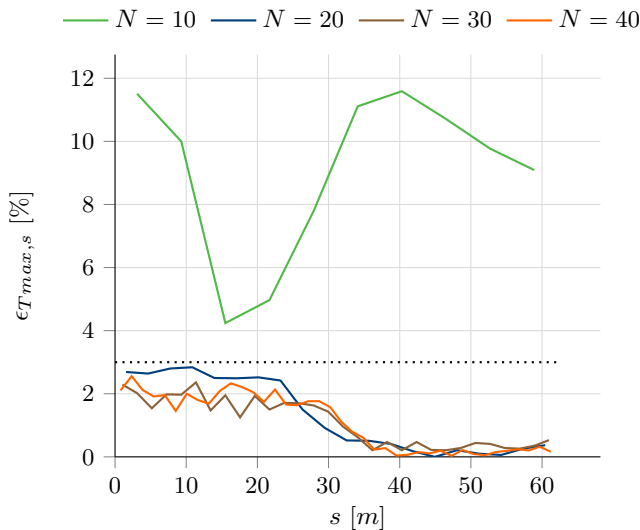


Figure 29: Dynamic error $\epsilon_{T_{max,s}}$ for various N . The acceptable error limit is indicated with the dotted horizontal line.

Figures 28 and 29 show that the discretization refinement should be $1.55m$ ($N = 40$ for $L = 62m$) or smaller for the dynamic discretization error to be acceptable. The two mentioned figures also indicate that the discrepancy between cases with a coarse and fine mesh at the minimum tensions is approximately two times larger than the discrepancy at the maximum tensions. The cause of these discrepancies has been found and is described in the following paragraphs.

The cases run with a coarse mesh have a larger l_0 and therefore also a larger mass per element. Additionally, the angle of the first element which touches down on the seabed when the cable motion is downwards is larger for cases with a coarser mesh. This larger angle at TDP is visualized in Figure 30, where a static cable configuration is plotted for 10 and 100 elements. A higher element mass contributes to a higher reaction force

from the seabed, and a higher touch-down angle causes a larger component of the seabed reaction force in the longitudinal direction of the cable element. The combination of these two phenomena causes a high compression force in the element which touches down on the seabed. The seabed damping force is highest when the downward velocity of a touching-down node is highest, which is the case when it first touches down; after that point in time the node is slowed down by the seabed. Therefore, the change in element tension is very rapid for coarse elements when these elements touch down. For convenient reference, the described phenomenon is called *touch-down compression waves*. This phenomenon is shown in Figure 31, in which the tension time history of an element near the TDP is plotted. As can be seen, a mesh with a coarser mesh shows more intense touch-down compression waves.

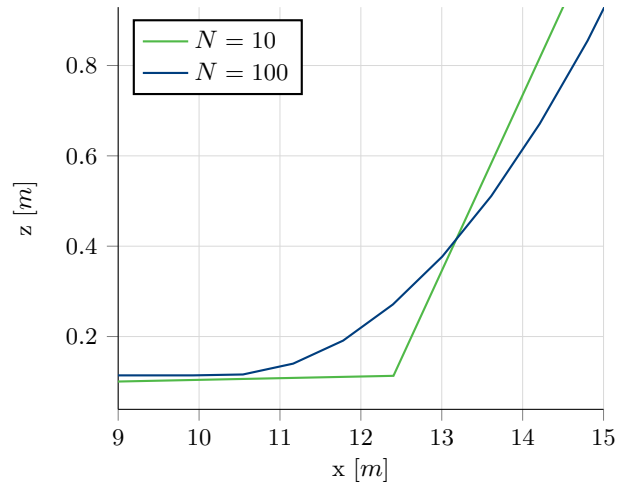


Figure 30: Static cable geometry near the TDP.

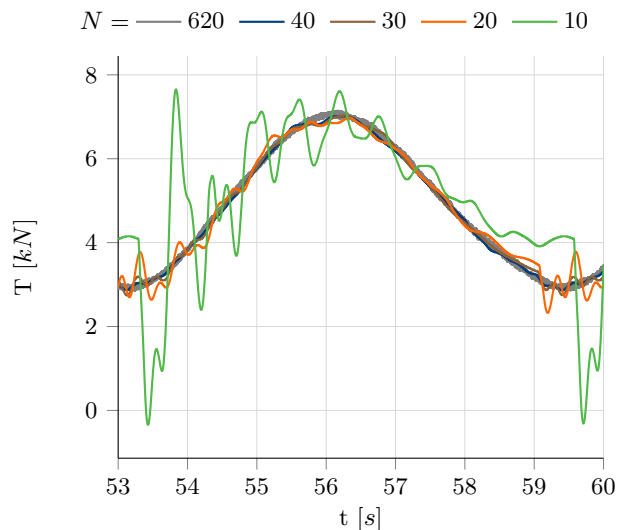


Figure 31: Tension time history at cable location $s = 12.45$ from $t = 53s$ to $t = 60s$. $T_{displ} = 2\pi s$.

After the initialization of a touch-down compression wave in the discretized cable, the wave travels towards the boundaries of the cable through the cable's longitudinal direction. Proof of this is shown in Figure 32, which shows the tension time history of an element near the departure point. The compression wave can be recognized by oscillations around the mean tension, and it arrives at $s = 49.55m$ a specific time interval after the initialization of the compression wave at the TDP. The travelling touch-down

compression wave can be visually detected with greater ease when one zooms into time. This has been done in Figure 33, which shows the tension at three points on the cable in the period where a touch-down compression wave is initiated. The cases shown in Figure 33 are defined in Section 5.2.

The speed of the compression waves has been analyzed, which resulted in the finding presented in Equation 70. Equation 70 shows that the measured longitudinal wave speed is dependent on cable properties and the discretization refinement l_0 . The terms shown in Equation 70 are outlined in Section 4.4.

$$c_{measured} = \frac{c}{\lambda} = \frac{c}{\sqrt{\hat{\beta}_{l_0}}} = \sqrt{\frac{EA}{\hat{\beta}_{l_0} \cdot (m + m_a)}} \quad (70)$$

When comparing Figures 31 and 32, it can be seen that the magnitude of the compression wave hardly decreased while traveling from $s = 12.45m$ to $s = 49.55m$. This can be explained by the fact that no tangential hydrodynamic drag and no structural damping have been modeled. The sole dissipation of energy in the modeled system happens because of normal hydrodynamic damping and seabed damping. The compression wave travelling from $s = 12.45m$ to $s = 49.55m$ is hardly exposed to normal hydrodynamic damping and not exposed to seabed damping.

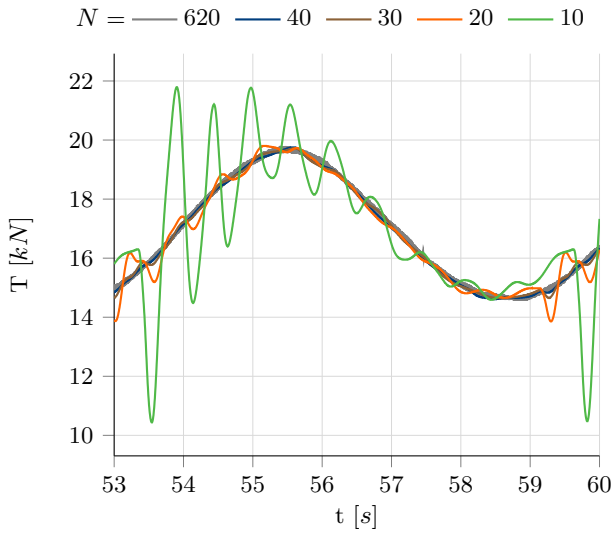


Figure 32: Tension time history at cable location $s = 49.55$ from $t = 53s$ to $t = 60s$. $T_{displ} = 2\pi$ s.

4.4. Model stability

As explicit time domain integration has been used in combination with a fixed timestep, the model is conditionally stable. The model stability is dependent on the timestep and on the speed with which longitudinal waves travel through the cable. This is a result of own research, as is the stability criterion which is presented in Equation 77. In the remainder of this section the stability criterion will be explained and proven to be correct.

Longitudinal waves travel through the thin rods with speed c , which is defined in Equation 71 [Metrikine and Vrouwenvelder, 2016]. As the cable is modeled as a sequence of thin rods, longitudinal waves are assumed to travel with speed c through the cable. In Equation 71, E and ρ are the Young's modulus and density of the cable, respectively. When both the numerator and denominator are multiplied with cable cross-sectional area A and unstretched cable element length l_0 , the denominator is equal to the inertial mass of one cable element.

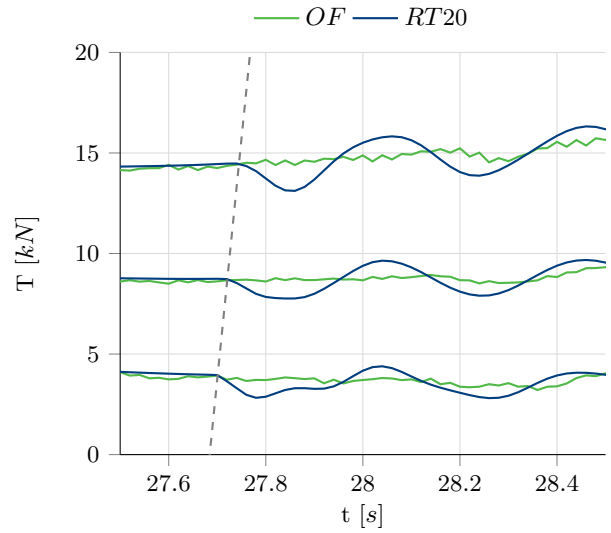


Figure 33: Tension time history at cable locations $s = 17.05m$ (bottom lines), $32.55m$ (middle lines) and $48.05m$ (top lines). The grey dashed line indicates that the touch-down compression wave is travelling upwards through the cable.

$$c = \sqrt{\frac{E}{\rho}} = \sqrt{\frac{EA}{\rho A}} = \sqrt{\frac{EA}{m_{inertia}}} = \sqrt{\frac{EA}{m + m_a}} \quad (71)$$

A longitudinal wave passing through random point P on the cable is visualized in Figure 34. The period t_{LW} in which the wave travels through one element of length l_0 is found by dividing the element length by the wave speed, as shown in Equation 72.

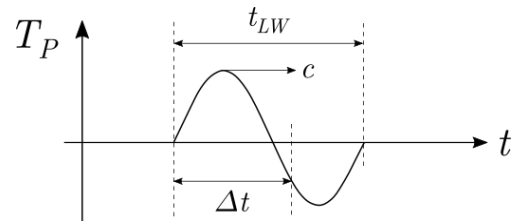


Figure 34: Tension at random point P in the cable given over time t . A longitudinal wave travels through the cable and passes point P with speed c .

$$t_{LW} = \frac{l_0}{c} = l_0 \cdot \sqrt{\frac{m + m_a}{EA}} \quad (72)$$

In order to model these longitudinal waves, the timestep used in the model Δt should be smaller than t_{LW} . This condition is given in Equation 73, where coefficient λ is defined as ratio $\frac{\Delta t}{t_{LW}}$. When Equation 72 is substituted into Equation 73, all terms are squared, Equation 12 is taken as inertial mass and the formula is rewritten for EA ; Equation 74 is found. Because coefficient λ^2 is dependent on unstretched element length l_0 and its square term is unnecessary, it is renamed to β_{l_0} .

$$\Delta t = \lambda \cdot t_{LW} = \sqrt{\beta_{l_0}} \cdot t_{LW} \quad (73)$$

$$EA = \lambda^2 \cdot \frac{(m + m_a)}{\Delta t^2} \cdot l_0^2 = \beta_{l_0} \cdot \frac{(m + m_a)}{\Delta t^2} \cdot l_0^2 \quad (74)$$

There is a certain maximum timestep Δt_{max} which can be used while still being able to model the longitudinal wave. When the timestep approaches Δt_{max} , the model error increases. When this timestep is exceeded, the model becomes unstable. This stability criterion is given in Equation 75.

$$\Delta t_{max} = \sqrt{\beta_{l_0,limit}} \cdot t_{LW} \quad (75)$$

Equation 75 can be rewritten for EA in the same way as Equation 73 was rewritten to 74. Instead of a maximum timestep now a maximum axial stiffness defines the criterion for model stability, as shown in Equation 76. Limit coefficient $\beta_{l_0,limit}$ is renamed to $\hat{\beta}_{l_0}$ here.

$$EA_{unstable} = \hat{\beta}_{l_0} \cdot \frac{(m + m_a)}{\Delta t^2} \cdot l_0^2 \quad (76)$$

Equation 76 can be converted into a stability criterion. This stability criterion is given in Equation 77 and is the final criterion of the presented derivation. The equation provides a simple approach for predicting the model stability based on: empirically found stability coefficient $\hat{\beta}_{l_0}$, cable mass per unit length m , added mass per unit length m_a , unstretched cable element length l_0 and timestep Δt .

$$EA \leq \hat{\beta}_{l_0} \cdot \frac{(m + m_a)}{\Delta t^2} \cdot l_0^2 \quad (77)$$

In order to determine stability coefficient $\hat{\beta}_{l_0}$, Equation 78 has been set up. The numerator contains the actual axial stiffness at which the model becomes unstable ($EA_{unstable}$) and the denominator contains an *uncorrected* axial stiffness limit ($EA_{uncorrected}$).

$$\hat{\beta}_{l_0} = \frac{EA_{unstable}}{\frac{(m+m_a)}{\Delta t^2} \cdot l_0^2} = \frac{EA_{unstable}}{EA_{uncorrected}} \quad (78)$$

Equation 78 has been evaluated for different cases in which the element length l_0 and timestep Δt have been varied. The cable and water properties used in all cases are equal: cable A (see Table 6) with a total length of $62m$ and $40m$ of water with a density of $\rho_w = 1025 \frac{kg}{m^3}$. Element length l_0 has been varied by changing the amount of elements N , while keeping $L = 62m$.

Intermezzo - Procedure for finding $EA_{unstable}$

The procedure for finding $EA_{unstable}$ is as follows: predict the approximate axial stiffness limit by calculating the denominator of Equation 78, multiply this value with $\frac{3}{4}$ and initiate the model with the resulting value (and a certain Δt and l_0). Then during runtime increase the axial stiffness of the cable, while exciting the cable dynamically, until the model becomes unstable. The axial stiffness at which the model becomes unstable ($EA_{unstable}$) has then been found and $\hat{\beta}_{l_0}$ can be calculated for the used combination of Δt and l_0 . Decreasing Δt and increasing N increases the computational expense of the model. This procedure can therefore be repeated until the maximum computational power of the computer on which the model is run is reached.

End of intermezzo

For each modeled combination of Δt and l_0 , a value for $\hat{\beta}_{l_0}$ was found. These values are given in Table 2. The cable has been excited dynamically by moving z -coordinate of the departure point (z_{DP}) over time with Equation 79, where $z_{DP,initial}$ equals the water depth of $40m$.

$$z_{DP} = \sin(t) + z_{DP,initial} \quad (79)$$

Table 2: Empirically found values for $\hat{\beta}_{l_0}$, for various combinations of Δt and l_0 where $L = 62m$ ($N = \frac{L}{l_0}$). Average $\hat{\beta}_{l_0}$ per l_0 is given. "Comp." means the model was limited by the computational power of the author's computer, which is given in Appendix A.3.

$\frac{1}{\Delta t}$ [Hz]	l_0 [m]			
	6.20	3.10	2.07	1.55
25	0.788	0.782	0.766	0.756
50	0.788	0.756	0.759	0.756
100	0.790	0.772	0.771	0.772
150	0.792	0.781	0.772	0.772
200	0.793	0.772	0.771	0.774
250	0.793	0.775	0.773	0.766
300	0.797	0.775	0.774	0.770
350	0.794	0.778	0.774	Comp.
400	0.794	0.777	Comp.	
450	0.792	Comp.		
500	0.794			
550	Comp.			
Avg.	0.792	0.774	0.770	0.767

As can be seen in Table 2, the value of $\hat{\beta}_{l_0}$ is relatively constant for a fixed element length and a varying timestep. Therefore, the average value of $\hat{\beta}_{l_0}$ for a fixed element length is assumed to be valid for that specific element length, regardless of the timestep. Increasing l_0 yields increasing $\hat{\beta}_{l_0}$, as shown in Figure 35. This means that cables which are modeled with a larger l_0 become unstable at higher values of EA .

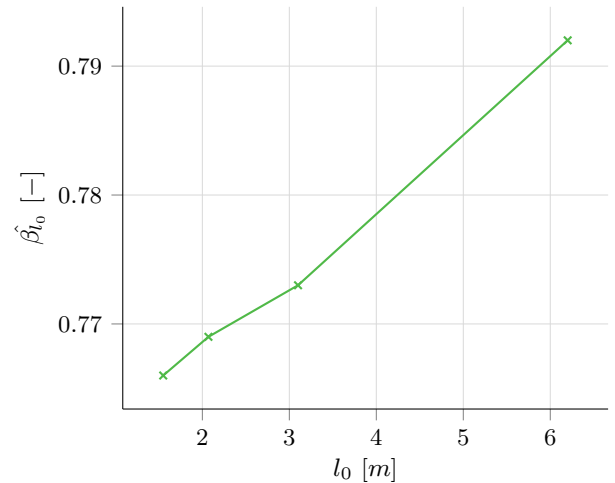


Figure 35: Coefficient $\hat{\beta}_{l_0}$ versus l_0 .

Stability coefficient $\hat{\beta}_{l_0}$ has been determined for four different element lengths. Therefore now the maximum axial stiffness for which the model is stable can be predicted for an infinite amount of timestep sizes and for different values of l_0 , using Equation 76 and Figure 35. When this is done, the *model stability graph* is created: see the solid lines in Figure 36.

The found values for EA at which the model becomes unstable are indicated with crosses in Figure 36 and are given in Table 3. As can be seen in Figure 36, the stability prediction from Equation 76 accurately matches the actual found stability.

In order to verify whether the values for $\hat{\beta}_{l_0}$ as presented in Table 2 are truly only dependent on l_0 , $EA_{unstable}$ has been predicted with Equation 76 for a cable with a different mass

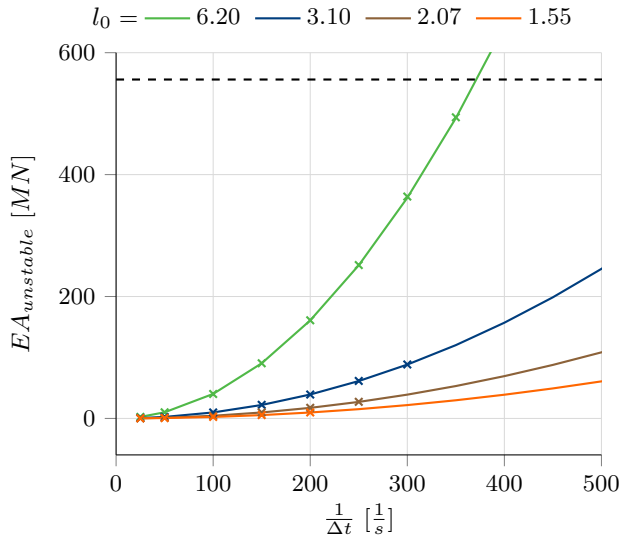


Figure 36: Model stability graph, indicating the maximum values of EA for which the model is stable for various values of l_0 . Solid lines are predictions from Equation 76. Crosses indicate the actual EA values at which the model becomes unstable. The horizontal dashed line indicates EA of cable A.

than cable A, but with the same values of β_{l_0} . Additionally, in another case L and N were increased while keeping l_0 equal. According to the procedure described in the above intermezzo, the actual values of EA for which the model becomes unstable are found for both cases. When these actual values are then compared to the predictions, the predictions are found to match accurately with the actual values of $EA_{unstable}$ again. Therefore, it can be concluded that Equation 76 is valid and that β_{l_0} is independent of cable (and added) mass.

4.5. Optimizing performance

The importance of the time required for computing the new cable state (t_{CPU}) for real-time modeling is outlined in Section 3. Time t_{CPU} is a function of: discretization refinement N , available computer power and model efficiency. Effort has been made to maximize the model efficiency in order to decrease t_{CPU} and thereby allow for a smaller model timestep, expanding the workable range of EA and N . The four specific measures taken to increase model efficiency are given in Sections 4.5.1 to 4.5.4.

4.5.1. Vectorization

In an early stage of the numerical model presented in Section 4.2 many operations were executed for a single value at a time, using *if*-loops. In the current version of the numerical model *vectorization* has been applied everywhere in the code. Vectorization is the process of revising loop-based code to use matrix and vector operations. *Vectorizing* your code is advantageous for code appearance and the risk of making errors while typing the code, but the most important advantage is its major (positive) impact on performance [Matlab, 2017]. Vectorization is also known as *array programming* and relies on the characteristic that operations can be directly applied to entire arrays of values, instead of to single values. Array programming is widely used particularly in the fields of science and finance [Mougin and Ducasse, 2003]. Although the increase in model performance due to vectorization has not been quantified, it is expected that

Table 3: Axial stiffness values from which the model is unstable. “Comp.” means the model was limited by the computational power of the author’s computer, which is given in Appendix A.3.

$\frac{1}{\Delta t}$ [Hz]	l_0 [m]			
	6.20	3.10	2.07	1.55
25	2.50	0.62	0.27	0.15
50	10.00	2.40	1.07	0.60
100	40.10	9.80	4.35	2.45
150	90.50	22.30	9.80	5.51
200	161.00	39.20	17.40	9.83
250	251.60	61.50	27.27	15.20
300	364.00	88.50	39.30	22.00
350	494.00	120.90	53.50	Comp.
400	645.00	157.70	Comp.	
450	814.00	Comp.		
500	1008.00			
550	Comp.			

t_{CPU} would increase with at least 50% when instead of vectorization *if*-loops were used. In light of its impact on performance, vectorization is considered as essential for real-time modeling.

4.5.2. Initial condition: catenary

When the model starts running a certain initial condition is given to the cable. This initial condition is typically not exactly equal to the equilibrium position of the cable, but differs from it to a certain degree. This difference defines the magnitude and duration of the cable movements to converge towards its equilibrium position. To minimize the mentioned magnitude and duration, an initial condition as close as possible to the expected equilibrium position is used. A catenary shape cable with a horizontal cable part (lying down on the seabed) attached to it is deemed as the optimal initial condition and is defined in Section 2.17. Impact on performance is a quicker convergence towards equilibrium.

4.5.3. Updating drag coefficient not every timestep

As outlined in Section 2.5.1, coefficient $C_{D,n}$ is dependent on relative cable element velocity V_p . During every model timestep Δt all variables are re-calculated. For updating $C_{D,n}$ the code computes Re and finds the corresponding $C_{D,n}$ using a polynomial curve of Figure 5. This process requires some computation expense, while it is not expected that $C_{D,n}$ is changing over time with the typical frequencies in which the real-time model is run (at 200Hz or higher). Therefore $C_{D,n}$ is updated every 10th timestep, yielding less computational expense and higher performance.

4.5.4. Lowering framerate

In an earlier stage of the real-time model, visualization frame duration t_{frame} was equal to model timestep Δt . As explained in Section 3.3, t_{frame} does not have to be equal to Δt . To this end ratio η has been set up. Increasing η from 1 (earlier stage of model) to 4 (current model) yields an increased performance, which is quantitatively shown in Figure 37. Performance increases with η because updating the visualization frame yields updating the position, orientation and color of all cable elements and nodes, which requires a specific computational expense.

$\frac{1}{\Delta t}$ [Hz]	l_0 [m]				$\frac{1}{\Delta t}$ [Hz]	l_0 [m]			
	6.20	3.10	2.07	1.55		6.20	3.10	2.07	1.55
25	2.50	0.62	0.27	0.15	25	2.50	0.62	0.27	0.15
50	10.00	2.40	1.07	0.60	50	10.00	2.40	1.07	0.60
100	40.10	9.80	4.35	2.45	100	40.10	9.80	4.35	2.45
150	90.50	22.30	9.80	5.51	150	90.50	22.30	9.80	5.51
200	161.00	39.20	17.40	9.83	200	161.00	39.20	17.40	9.83
250	251.60	61.50	27.27	Comp.	250	251.60	61.50	27.27	15.20
300	364.00	88.50	Comp.		300	364.00	88.50	39.30	22.00
350	494.00	Comp.			350	494.00	120.90	53.50	Comp.
400	645.00				400	645.00	157.70	Comp.	
450	814.00				450	814.00	Comp.		
500	Comp.				500	1008.00			
					550	Comp.			

Figure 37: Table 3 with $\eta = 1$ (left) and $\eta = 4$ (right).

4.6. Sensitivity analysis: modeling a lower EA

It is shown in Section 4.4 that in order to achieve numerical stability, the axial stiffness which can be modeled in real-time is limited. Even though the model performance has been optimized as described in Section 4.5, the workable range of EA is not wide enough to model EA values of most of the typical export and infield cables given in Appendix A.2 with an acceptable error. This problem can be circumvented by either using a stronger computer than the computer given in Appendix A.3 or by modeling the cable with a lower axial stiffness. The current section studies the impact on the model results of the latter option.

The approach of the sensitivity analysis entails an analysis of the dynamic tension results for cable A from Table 6 with $L = 62m$, $d = 40m$, $k_{soil} = 100 \frac{kN}{m}$ and $l_0 = 0.5m$. The error resulting from modeling a lower EA than the actual EA specified by the cable manufacturer is analyzed in an analogous way to the dynamic discretization error analysis given in Section 4.3.2. The cable is excited dynamically by a harmonic movement in z -direction of the departure point. The mentioned harmonic displacement is given by Equation 66, where $\omega_{displ} = 1 \frac{rad}{s}$ yielding $T_{displ} = \frac{2\pi}{\omega_{displ}} = 6.283s$. Four cases have been defined, in which EA and A_{displ} are varied. These cases are given in Table 4 and have been run in OrcaFlex. The harmonic wave simulated by the harmonic movement of the departure point has wave height $H = 2 \cdot A_{displ}$.

Table 4: Cases analyzed for the sensitivity analysis of EA . Parameter ξ indicates the percentage of the axial stiffness of cable A .

Case	EA [MN]	ξ [%]	A_{displ} [m]	H [m]
1	556	100.0	0.5	1.0
2	22	4.0	0.5	1.0
3	556	100.0	1.25	2.5
4	22	4.0	1.25	2.5

Two values of EA are defined in the cases given in Table 4. Cases 1 and 3 apply the EA of export cable A . Cases 2 and 4 apply the maximum EA which can be modeled in the real-time model for $l_0 = 1.55m$, which is the discretization refinement required for the dynamic discretization error to be acceptable as described in Section 4.3.2. A relatively calm seastate is simulated in cases 1 and 2, with $H = 1m$. Typically the workability of cable lay vessels limits the workable significant wave height at $2.5m$, which is why this relatively severe wave height is applied in cases 3 and 4. Tension range graphs analogous to the tension range graphs in Section 4.3.2 have been constructed for these cases and are shown in Figures 38 and 39.

Error resulting from modeling a lower EA is defined for min-

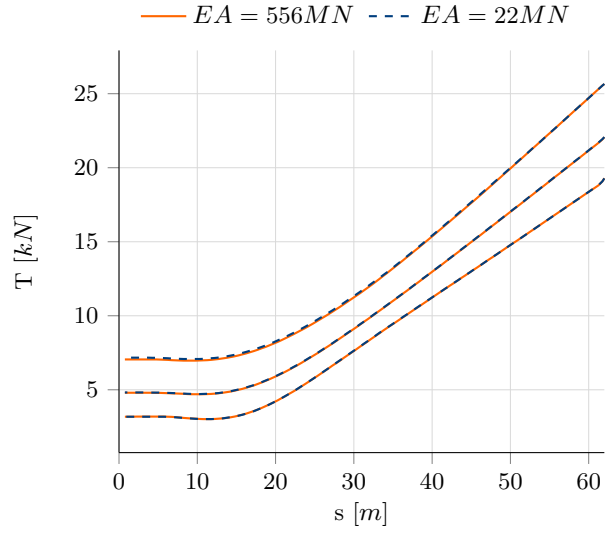


Figure 38: Tension range graph showing the minimum (bottom lines), mean (middle lines) and maximum tension (top lines) along the cable length for $H = 1.0m$ from $t = 53s$ to $t = 60s$.

imum, mean and maximum tension by Equations 80 to 82. Equation 80 divides the absolute error by the mean tension instead of minimum tension to avoid extremely high relative errors when $T_{min,s}$ approaches zero. Dimensionless errors $\varphi_{Tmin,s}$, $\varphi_{Tmean,s}$ and $\varphi_{Tmax,s}$ have been plotted in Figures 40 and 41.

$$\varphi_{Tmin,s} = \frac{|T_{min,s,22} - T_{min,s,556}|}{T_{mean,s,556}} \cdot 100\% \quad (80)$$

$$\varphi_{Tmean,s} = \frac{|T_{mean,s,22} - T_{mean,s,556}|}{T_{mean,s,556}} \cdot 100\% \quad (81)$$

$$\varphi_{Tmax,s} = \frac{|T_{max,s,22} - T_{max,s,556}|}{T_{max,s,556}} \cdot 100\% \quad (82)$$

It can be concluded that the differences in dynamic tension for 556MN and 22MN are marginal by visual inspection of Figures 38 and 39. Figures 40 and 41 show that the maximum error φ_s along the cable length is 1.67% for $H = 1.0m$ and 2.05% for $H = 2.5m$.

5. Verification and validation

The current chapter presents two different analyses to verify whether the created numerical model described in Section 4 is implemented correctly. An analytical verification is given in Section 5.1. The performed validation with industry-standard software is outlined in Section 5.2.

5.1. Analytical verification of static state

In a static situation where the axial and bending stiffness of the cable can be neglected, the geometry of a suspended cable is governed by product weight only. The cable's geometry corresponds to a half catenary in this case, which can be described by a hyperbolic cosine function. Using the analytically derived catenary formulas from [DNV GL, 2015] the product geometry can be estimated. Equations 83 to 85 are used, where a is a calculation constant, T_{bot} is bottom tension (at TDP), m_{sub} is the submerged cable weight, s is the arc distance from origin

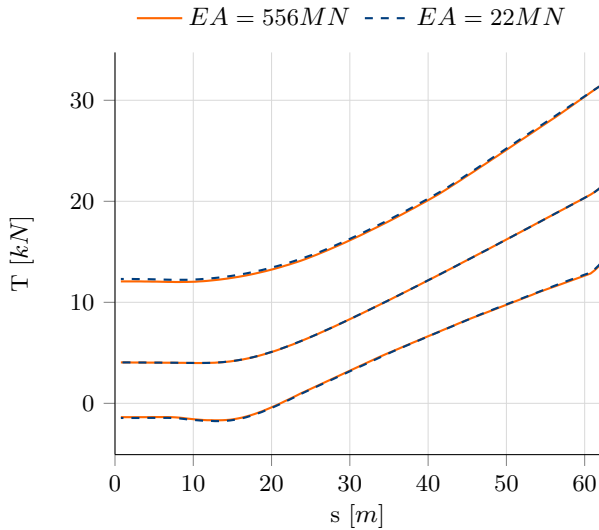


Figure 39: Tension range graph showing the minimum (bottom lines), mean (middle lines) and maximum tension (top lines) along the cable length for $H = 2.5m$ from $t = 53s$ to $t = 60s$.

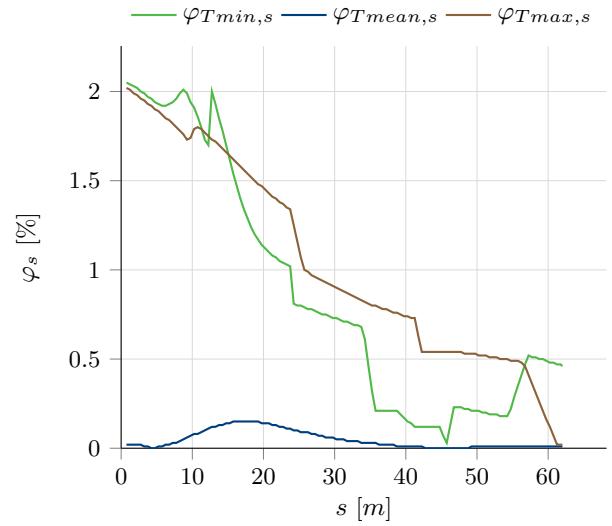


Figure 41: Dynamic tension errors φ_s for $H = 2.5m$.

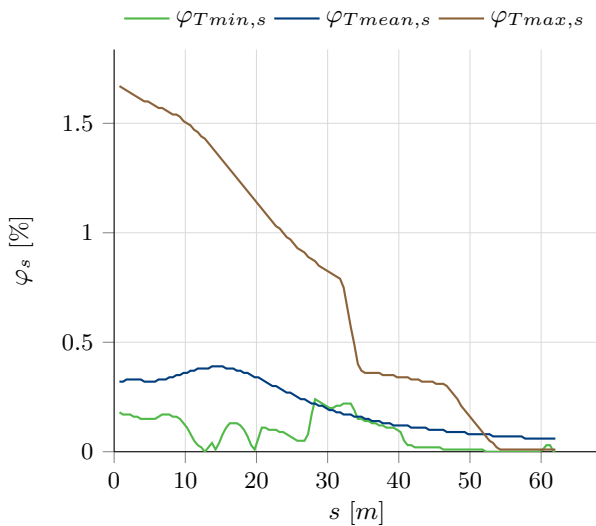


Figure 40: Dynamic tension errors φ_s for $H = 1.0m$.

and x and z are the horizontal and vertical coordinate of the cable at arc distance s , respectively.

$$a = \frac{T_{bot}}{m_{sub} \cdot g} \quad (83)$$

$$x(s) = a \cdot \sinh^{-1}\left(\frac{s}{a}\right) \quad (84)$$

$$z(s) = \sqrt{a^2 + s^2} - a \quad (85)$$

The static case for which the results from the numerical solution will be verified has a water depth of $40m$ and models subsea power cable A (see Table 6), both of which are typical for a North Sea cable installation project. The cable is assumed to be fully submerged and in the numerical solution the cable is split up into 20 elements. Bending stiffness is set to zero. The numerical solution provided a bottom tension of $7.78kN$, which is put into Equation 83 in order to compute the analytical solution. The resulting cable geometry from the numerical and analytical solutions are shown in Figure 42.

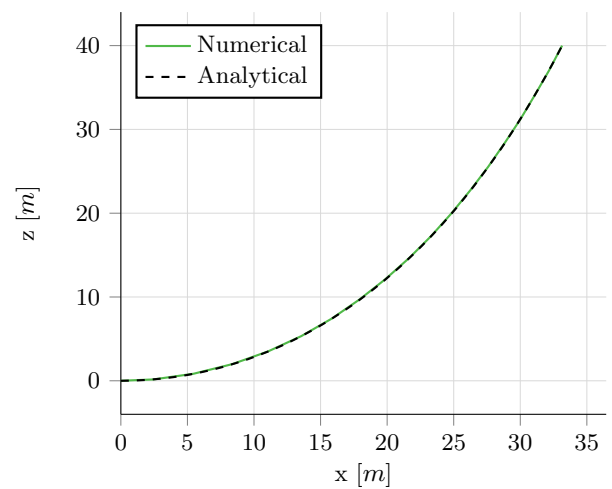


Figure 42: Cable geometry from the numerical and analytical static solutions.

Complementary to the visual verification an exact verification has been done. This is done by finding the z -coordinate of the analytical solution exactly on the x -location of a node from the numerical solution. As z is a function of s in the analytical solution, first arc distance s corresponding to the numerical x -coordinate has to be found. Therefore, the numerical x -coordinate for a node is substituted into Equation 84 after which the equation is solved for s . The found arc distance is substituted into Equation 85, resulting in the analytical z -coordinate. Then the absolute difference between the z -coordinate from the analytical and numerical solution is calculated. The described procedure has been executed for every node on the suspended cable. The maximum found absolute difference between the numerical and analytical z -coordinates is $4.3cm$, which equals $0.18D$. As this value is relatively small in comparison with the cable length of $55m$, it is concluded that the geometry found with the numerical solution is analytically verified.

As complementary verification, true tension found by the numerical model will be analytically verified. As no current is present in the static case under consideration, only cable weight contributes to the change of tension in the cable. The vertical component of the tension at any point along the suspended cable should therefore be equal to the weight of the cable up to that point. The force diagram and vertical force balance of the

static case are given in Figure 43 and Equation 86, respectively. Angle θ is the angle between the cable longitudinal axis and the vertical.

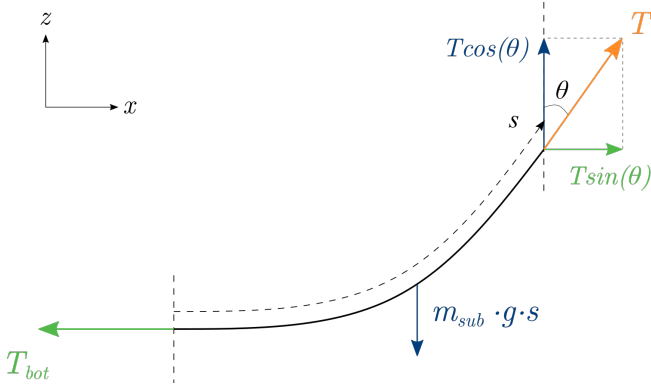


Figure 43: Force diagram of a static suspended cable case.

$$\sum F_z : T \cos(\theta) - m_{sub} \cdot g \cdot s = 0 \quad (86)$$

The true tension in the any element of the numerical solution represents the average tension of that element, and is calculated by multiplying the strain of that element by the axial stiffness (Equation 2). As the numerically found tension represents the average tension of the element, the vertical component of the tension should be equal to the weight of all elements hanging from that element plus half the weight of the element itself.

The numerical solution finds a true tension of $24.3kN$ in the upper element of the cable, while θ equals 18.4 degrees here. Arc distance s halfway the upper element was found by substituting the x -coordinate of its midpoint into Equation 84 and solving for s , yielding an arc distance of $53.6m$. To verify the numerically found tension, the result of Equation 86 should equal zero, which for this case is verified in Equation 87.

$$\begin{aligned} T \cos(\theta) - m_{sub} \cdot g \cdot s &= 24.3(10^3) \cdot \cos(18.4^\circ) \\ &\quad - 43.92 \cdot 9.81 \cdot 53.6 \\ &= 28.6 \text{ [N]} \end{aligned} \quad (87)$$

The numerical and analytical solution are thus offset by $28.6N$ for the upper element. The above verification has been done for all elements of the numerical static case. The maximum absolute offset found is $92.4N$, which is 0.4% of the vertical component of the tension at the corresponding element. As this is a marginal difference, the numerical true tension is hereby deemed as analytically verified.

Marginal differences found between the numerical and analytical solutions can be explained by the fact that the numerical solution includes axial stiffness, while the analytical solution disregards it. This yields that in the numerical solution the cable stretches due to the forces applied, while in the analytical solution the cable is inextensible.

5.2. Validation of dynamic state

For validating whether the model represents reality to an acceptable degree, real-world experiments are preferred. Real-world experiments are both costly and time-consuming. Therefore, the model has been validated using the world's leading package for dynamic analysis of offshore marine systems: *OrcaFlex*. *OrcaFlex* is assumed to accurately represent reality as it is the industry standard for, among other analyses, dynamic subsea

cable analysis. The validation is focused on two key parameters which dictate the cable state during installation: (effective) tension and geometry. Section 5.2.1 defines the dynamic case which has been validated. In Sections 5.2.2 and 5.2.3 the tension and geometry are validated, respectively. A reflection on the performed validation is given in Section 5.2.4.

5.2.1. Validation case

For validation of the real-time model results cable *A* from Table 6 is used with $EA = 50MN$, $L = 62m$, $d = 40m$ and $k_{soil} = 100 \frac{kN}{m}$. The cable is excited dynamically by harmonically moving the departure point in vertical direction with the displacement defined by Equation 88, where $A_{displ} = 0.5m$ and $\omega_{displ} = 1 \frac{rad}{s}$ yielding $T_{displ} = \frac{2\pi}{\omega_{displ}} = 6.283s$. Two cases have been run in the real-time model and one case has been run in *OrcaFlex*, as given by Table 5.

$$z_{DP} = A_{displ} \cdot \sin(\omega_{displ} \cdot t) + z_{DP,t0} \quad (88)$$

Table 5: Validation cases in real-time (RT) and *OrcaFlex* (OF) models.

Reference	RT20	RT30	OF
N	20	30	20
l_0 [m]	3.1	2.07	3.1

5.2.2. Dynamic tension validation

Tension results are presented by the tension range graph given in Figure 44. Additionally the tension time history for three locations on the cable is plotted in Figure 45.

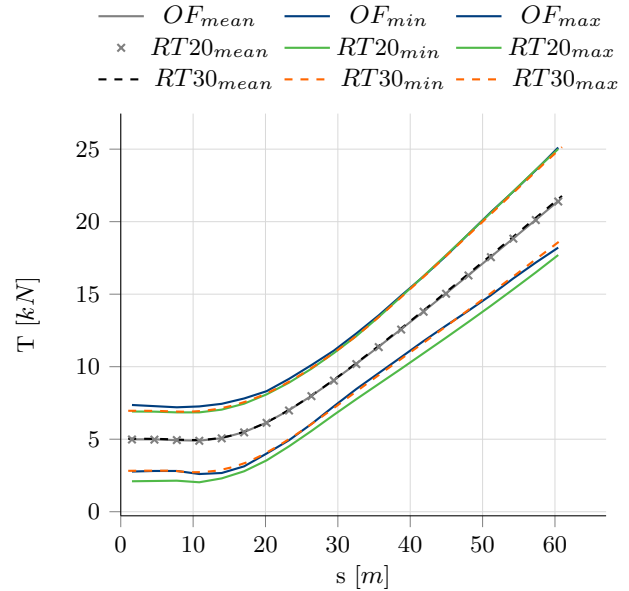


Figure 44: Tension range graph showing the mean, minimum and maximum tension along the cable length from $t = 20s$ to $t = 40s$.

5.2.3. Dynamic geometry validation

While excited dynamically the cable will oscillate around its equilibrium position i.e. its static geometry. To ensure a validation based on the same starting point i.e. the same static

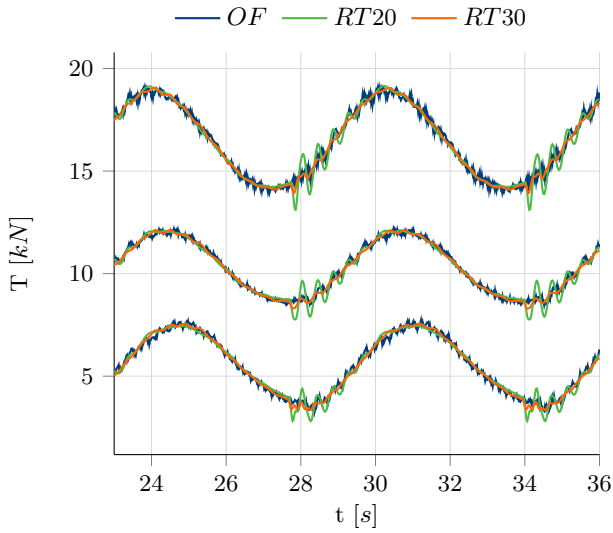


Figure 45: The three bottom, middle and top lines show the tension at $s = 17.05m$, $s = 32.55m$ and $s = 48.05m$.

geometry, first the static geometry of the cable is validated. The static cable geometry is given in Figure 46 for validation cases *RT20* and *OF*. The dynamic cable geometry has subsequently been validated in the same way as the dynamic geometry of a mooring line has been experimentally validated by [Azcona et al., 2017]. In the mentioned work, the dynamic geometry is validated by plotting the computed and experimental trajectory of specific points on the mooring line. Likewise, trajectory plots showing the motion of three points on the cable according to the three cases given in Table 5 are created. The trajectory plots are given in Figures 47 to 49.

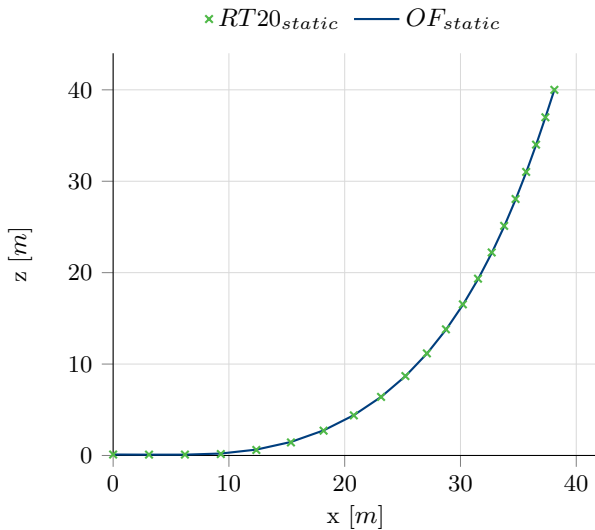


Figure 46: Static cable geometry.

5.2.4. Reflection on validation

Figure 45 shows that the discrepancy between the minimum tensions for *RT20* and *RT30* shown in Figure 44 are resulting from the relatively large touch-down compression waves in *RT20*. The concept of touch-down compression waves is explained in Section 4.3.2. The mean tensions plotted in Figure 44 show good agreement for all cases. The static cable geometries from *RT20* and *OF* match accurately as shown in Figure 46. The

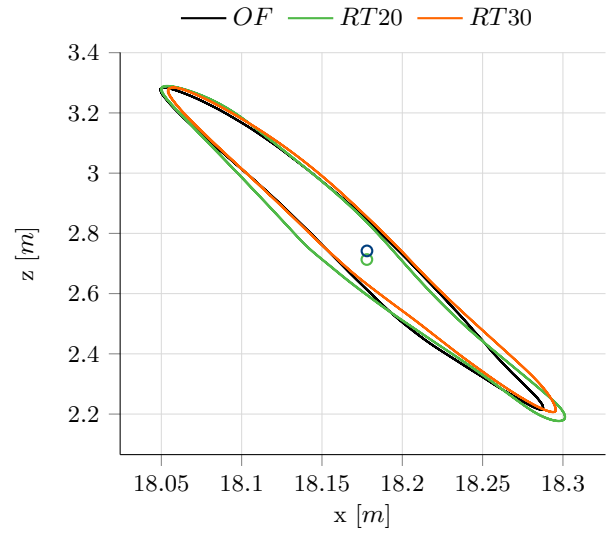


Figure 47: Trajectory of cable at $s = 18.6m$ from $t = 20s$ to $t = 40s$. The blue and green circles centered in the trajectories indicate static position in *OF* and *RT20*.

cable trajectories plotted in Figures 47 to 49 show differences between geometry smaller than the acceptable error defined in Section 2.1, which is $0.117m$ for cable *A*.

The maximum tensions in Figure 44 show a relatively small discrepancy between the real-time model and OrcaFlex results, mainly at $s \leq \frac{1}{2}L$. Also, no touch-down compression waves are found in the OrcaFlex results even though the OrcaFlex case has $N = 20$, like *RT20*. The latter two mentioned differences between real-time and OrcaFlex results are expected to be caused by the difference in time domain integration scheme used in the two models. Both models use an explicit method and a constant time step, but the real-time model uses a fourth order Runge-Kutta solver while OrcaFlex uses a semi-implicit Euler scheme [Orcina Ltd., 2017].

6. Visualizing in Augmented Reality

The thesis objective is to visualize the results of the real-time cable model into AR. Software choices made to this end are outlined in Section 6.1. The created user interface displays the cable using various colors which are used for data interpretation. The used color codes are defined in Section 6.2. The created user interface can be implemented in AR and is described in Section 6.3. Available AR hardware is given in Section 6.4.

The current work is the first work to publicly investigate the proposed application of AR during offshore cable lay. The status quo of AR is given in Appendix A.4. The proposed AR interface can act as a first step for further implementation. An implementation plan is recommended in Section 11.

6.1. Unity and C#

A multi-criteria analysis (MCA) has been carried out in order to find the most suitable programming language to build the real-time model and the most suitable software to realize the visualization in AR. The analysis scored various candidates on: ability to process real-time in- and outputs, ability to perform vector / matrix calculations, availability of ODE solvers and capability of visualizing model results in an AR interface. The candidates were also scored on non-technical aspects like

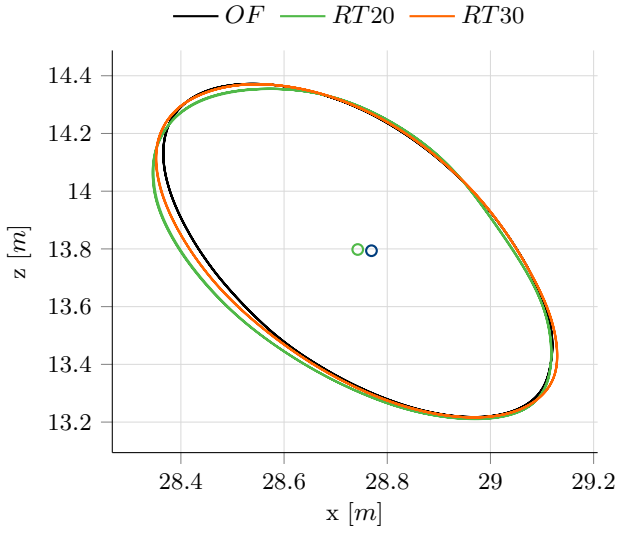


Figure 48: Trajectory of cable at $s = 34.1m$ from $t = 20s$ to $t = 40s$. The blue and green circles centered in the trajectories indicate static position in OF and RT20.

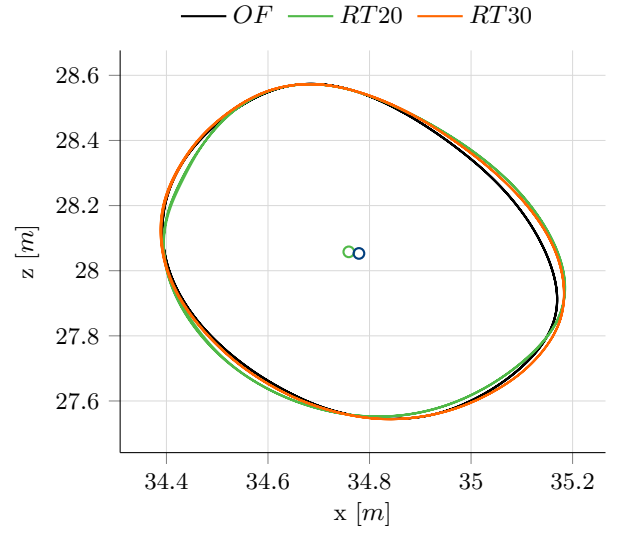


Figure 49: Trajectory of cable at $s = 49.6m$ from $t = 20s$ to $t = 40s$. The blue and green circles centered in the trajectories indicate static position in OF and RT20.

financial costs, available online documentation and required learning effort for the author to work with the candidate. The MCA indicated a combination of Unity and C# as the most suitable candidate.

Unity is a game engine with an extensive graphics library and a user-friendly interface. The AR hardware suggested in Section 6.4 works with Unity, ensuring that visualization in AR is relatively simple. C# is a mid-range programming language and is the scripting language of Unity. The Unity and C# (Microsoft Visual Studio) interfaces have been closely aligned to each other, making working with them simultaneously a seamless process.

6.2. Color codes

Model results are cable geometry and tension. These results are visualized in real-time by giving the discretized cable elements specific colors. The created AR interface has two modes: bending radius mode and tension mode. A color code is defined for each mode in Sections 6.2.1 and 6.2.2.

6.2.1. Bending radius mode

A safe, warning, critical and damage zone is defined for the bending radius. Each zone is visualized using different colors, as shown in Figure 50. One of the structural limits of a cable is its MBR. In case the cable is bend below the MBR, structural damage is likely to have occurred and therefore bending radii lower than the MBR are in the damage zone. When the bending radius of the cable is above the MBR, the cable's structural state is not compromised due to bending and the bending radius is in the safe zone. The warning and critical zones are created in order to warn the end-user of the AR interface in case the bending radius gets close to its structural limit. The warning margin is a user input of the model, allowing for project- or user-specific color code behaviour, and can be set to e.g. $5m$. The MBR of cable A from Table 6 is $3.6m$, yielding that the user will get visual warnings when the bending radius becomes smaller than $8.6m$, in this example.

As mentioned in Section 2.1 some errors (deviations from reality) have been consciously allowed into the model results, by

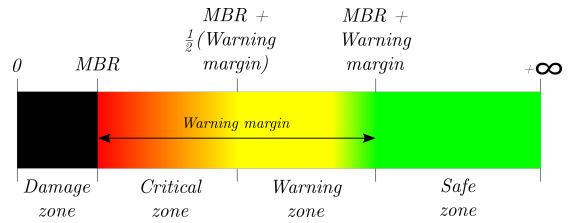


Figure 50: Bending radius mode color code.

disregarding physical phenomena. Additionally discretization errors are present as described in Section 4.3. To account for the made model errors a safety margin is added to the MBR which is specified by the cable manufacturer (from here on referred to as MBR_{cable}). It is assumed that the accumulated model error (resulting from disregarding physics and discretization) is equal to the acceptable error defined in Section 2.1 which for geometry is $0.5D$. In regards to the bending radius safety margin, it is assumed that the geometry error of $0.5D$ affects the bending radii computed by the model in the most disadvantageous way. In that case, the model would report the lowest bending radius in the cable to be e.g. $3.717m$ (= no damage) while in reality the bending radius at that cable location actually is $3.6m$ (= damage). The difference between the reported and actual lowest bending radius is equal to $0.5D$ (for cable A). This explanation is supported by Equation 89 and Figure 51.

$$MBR = MBR_{cable} + 0.5D \quad (89)$$

6.2.2. Tension mode

Similar to the color code made for the bending radius mode in Section 6.2.1, a color code is created for the tension mode. The tension mode color code is given in Figure 52. The tension can be in the damage zone because of either compression or overstretching of the cable. To enable the end-user of the AR interface to distinguish between compression and overstretching these damage zones are indicated with white and black, respectively.

Analogous to the assumption made in Section 6.2.1, it is assumed that the accumulated model error is equal to the ac-

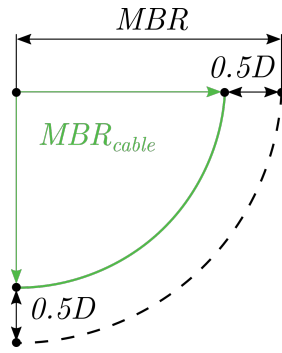


Figure 51: MBR Safety margin to account for model error.

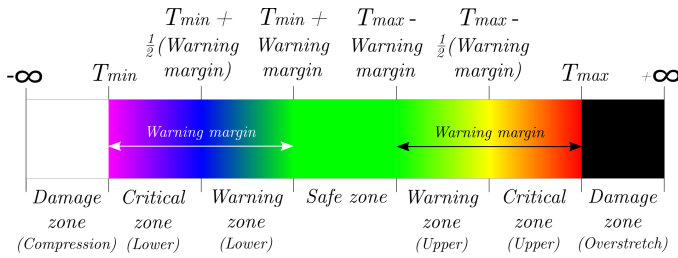


Figure 52: Tension mode color code.

ceptable error defined in Section 2.1, which for tension is 3%. In regards to the tension safety margin, it is assumed that the tension error of 3% affects the tension computed by the model in the most disadvantageous way. The cable element tension is first adjusted with the safety margin before it is given a color based on Figure 52. The adjusted tension is referred to as T_{color} and is calculated using Equation 90.

$$T_{color} = \begin{cases} T \cdot 0.97, & T \leq \frac{1}{2} \cdot (T_{max} + T_{min}) \\ T \cdot 1.03, & T > \frac{1}{2} \cdot (T_{max} + T_{min}) \end{cases} \quad (90)$$

6.3. AR interface

The created interface, which presents the model results in real-time, can be visualized on a computer screen and in AR. The interface on a computer screen is shown for cable A with $d = 40m$ and $N = 40$ in Figure 53. The AR interface for the same case is shown in Figure 54. The latter figure shows the perspective of a person using the AR hardware described in Section 6.4, standing next to the chute of a cable lay vessel. The model is in tension mode in both figures.

6.4. AR hardware

During the current research a collaboration has been set up with AR hardware producer DAQRI, resulting in the availability of the DAQRI Smart Glasses (DSG). The DSG, shown in Figure 55, is one of the first wearable AR devices which only recently (November 7th, 2017) became commercially available [Medium, 2017]. The lightweight pair of glasses and a small processing unit should be worn by the user, as shown in Figure 56. When the digital position of the cable matches its physical position from the perspective of the person wearing the DSG, that person is enabled to *look through the water*, as shown in Figure 54. The research done in the current thesis proves that the idea outlined in Section 1 is realizable with technology available at the time of writing.

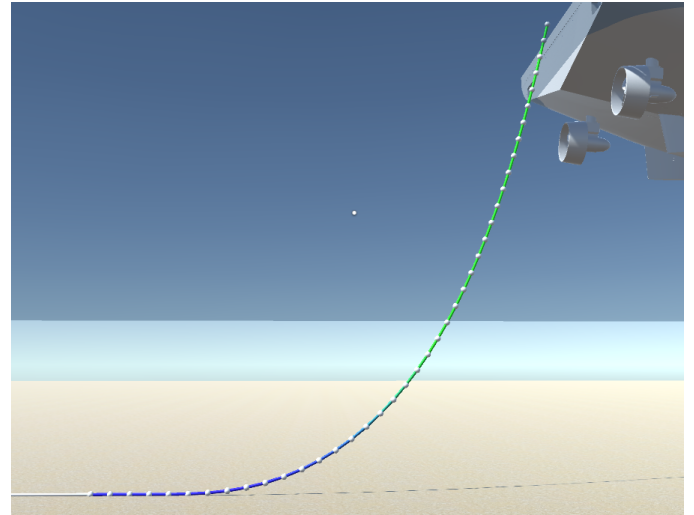


Figure 53: Visualization of the real-time model results on a computer monitor.

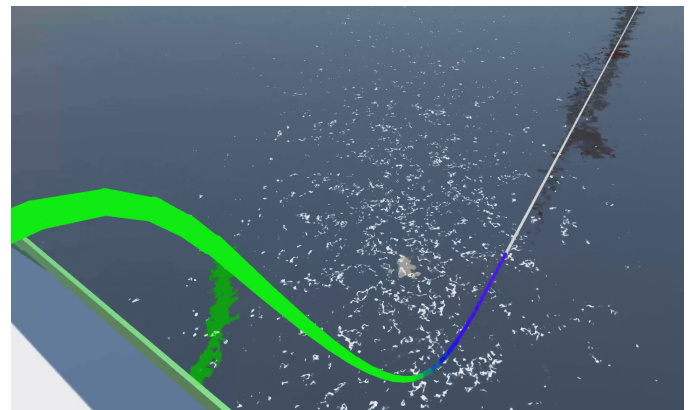


Figure 54: Visualization of the real-time model results through AR, enabling the user to look through the water.

7. Collaboration with Tilburg University - Legal aspects of AR in offshore cable lay

The scope of the current work is not limited to technical aspects. Additionally, research is done into the legal aspects of the idea of applying AR in the offshore cable laying process. As the author of the current work has a technical background, the legal aspects are investigated by an external team of people: an international group of four students from *Tilburg Institute for Law, Technology and Society* (TILT). These four students from Tilburg University put in 256 man-hours to complete their investigation during the so-called *Tideway-TILT Clinic* spread out over four weeks. The TILT group has been supervised by Tomasso Crepax from Tilburg University (for ensuring quality from Tilburg University's perspective) and the author of the current thesis paper (for ensuring a sufficient level of understanding of the technical aspects at the TILT group and for providing the group with all required technical information). The efforts of the TILT group yield a 32 page report, which outlines potential legal issues related to applying AR in the cable lay process. The full TILT report can be found in the references [Geer et al., 2017] and the paragraph below highlights the main *Tideway-TILT Clinic* results.

Use of AR creates the need to establish factors such as au-



Figure 55: State-of-the-art wearable AR device: *Daqri Smart Glasses* [DAQRI, 2017].

thority through contract even though there are no changes with regard to liability for employees when AR is implemented. It is strongly recommended to lay out obligations, expectations and intended use of the AR system in contract to protect Tideway from liability if damage were to occur. In regards to meeting the stringent safety standards typical in the offshore installation industry, following the International Maritime Organization code and implementing a Safety Management System plan with concessions for AR technology in mind is the best course of action to ensure successful implementation of this innovation. An adjustment to the existing cable lay insurance policy is advised, which would supplement it with a new version of Tideway’s cable laying guideline [Tideway Offshore Solutions, 2016] including the process of the AR application.

The added value of the TILT report relies in that the current research now identifies various potential legal issues which might form obstacles in the realization of the proposed innovation (applying AR in offshore cable installation). These potential legal issues are not definitively solved by the TILT report, but steer potential follow-up research or practical implementation of the proposed AR system into the right direction. The TILT report adds to the completeness of the current research and acts as a good starting point for follow-up legal research into AR in offshore cable lay.

8. Results

It was found that the following physics are required for modeling the dynamics of a typical subsea export cable which is installed in 40m of water depth with model errors below 0.5D displacement and 3% tension: gravity, buoyancy, normal hydrodynamic drag, seabed, inertia, added mass and bending stiffness. The following physics can be neglected without inducing model errors above 0.5D displacement and 3% tension: axial stiffness, direct effect of waves, tangential hydrodynamic drag, vessel sailing during cable lay, paying out cable during cable lay, aerodynamic drag, torque moments and structural damping. For defining the boundary and initial conditions at model start-up, vessel MRU and DAMS measurements are required. The same measurements are necessary for updating the BCs and ICs during model runtime after operational changes in layback length.

A cable dynamics model with an explicit method, a fourth-order numerical ODE solver and a fixed timestep has been created using freely available software. The model is conditionally stable and for numerical stability the timestep is required



Figure 56: The DSG demonstrated by the author.

to satisfy the following condition:

$$\Delta t \leq \sqrt{\hat{\beta}_{l_0} \cdot \frac{(m + m_a)}{EA} \cdot l_0^2}$$

Modeling the cable as stretchable instead of inextensible increases the model accuracy with 0.18D displacement and 0.4% tension for a static case and simplifies the numerical challenge of computing tension. Increasing axial stiffness requires a smaller timestep for numerical stability. The created model approaches real-time representation with a delay of several milliseconds. The consequence of modeling in real-time is that the average time taken to compute the cable state at the next timestep (\bar{t}_{CPU}) should be smaller than or equal to the model timestep itself. Duration \bar{t}_{CPU} is a function of amount of cable elements, available computer power and efficiency of the numerical model. Thereby, the axial stiffness which can be modeled in real-time is limited by the available computational resources. To circumvent this problem, the axial stiffness of a typical export cable has been lowered to a value which can be modeled in real-time. This value is 96.0% lower than the cable’s actual EA . A sensitivity analysis shows that modeling an axial stiffness which is 96.0% lower than the actual cable EA induces a maximum dynamic tension error of 1.67% for $H = 1.0m$ (relatively calm seastate) and 2.05% for $H = 2.5m$ (relatively severe seastate).

In order to keep static discretization errors below 0.5D displacement and 3% tension for a cable with a length of 62m, the cable should be discretized with at least 20 elements. To ensure that dynamic discretization errors are smaller than the mentioned errors, the cable should be discretized with at least 40 elements. The amount of elements should be higher when dynamic results are demanded because spurious touch-down compression waves occur and yield an unacceptable discretization error when less than 40 elements are used. The model however gives acceptable mean dynamic tension results when at least 10 elements are used.

High-end graphic visualization of the real-time model results has been realized with freely available software. The combination of a numerical model in C# and graphical visualization in Unity allows for displaying the real-time model results in currently available wearable AR hardware. To this end an AR user-interface has been developed.

9. Discussion

The current work presents an overview of which physics are relevant for modeling the dynamics of a subsea cable. A conclusion has been drawn for each separate form of physics based on own quantitative research, except for conclusions drawn about the direct effect of waves. The exclusion of the direct effect of waves is based on assumptions made by [Pinto, 2007]. The current work shows that for the case analyzed the tangential hydrodynamic drag force is negligible, even though [DNV GL, 2017] is inconclusive about this for cable laying in relatively shallow waters. Results indicate that vessel MRU and DAMS measurements are required to define and update the model BCs and ICs. As the two mentioned measurement instruments are typically present on cable lay vessels, no extra costs for acquiring these measurements are foreseen.

Modeling the cable as stretchable and thereby including axial stiffness is in line with relatively recent works in which cable dynamics are modeled, like [Pinto, 2007] and [Lacarbonara and Pacitti, 2008]. The described consequence of real-time modeling yields that the usable combination of model timestep and amount of cable elements is limited by available computer power. For modeling a given axial stiffness (EA) in combination with a certain cable element length (l_0), the model timestep cannot exceed a specific value as otherwise numerical instability occurs. This means that the maximum axial stiffness which can be modeled for a given amount of elements is limited by available computer power. Maximum axial stiffness values which can be modeled in real-time for various amounts of elements are given in Table 3. As shown by the sensitivity study on EA , modeling an axial stiffness which is feasible in the real-time model with an element length that gives acceptable dynamic discretization errors (this EA is 96.0% lower than the actual EA of cable A) induces an maximum error in the dynamic tension of 2% for a relatively severe seastate. This error is small in comparison to the decrease in EA and according to the definition of an acceptable error in Section 2.1, this error is acceptable. A stable numerical cable dynamics model was developed by [Pinto, 1995] using an implicit method. The current work shows that cable dynamics can be modeled in real-time using an explicit method and that overcoming the associated limitation on axial stiffness does not lead to inaccurate results.

One of the results of the current work is the AR user-interface. When the AR-interface is used by wearing an AR headset, the user is enabled to look through the water. For example a cable lay supervisor or a marine warranty surveyor can use this innovation to see the cable hanging from vessel to seabed, where cable colors indicate the structural state of the cable. Visualizing the structural state of the cable on the physical cable itself with AR could draw the operator's attention quickly to the most critical part of the operation, reducing the response time of the operator. Operational plans like a route corridor could be put into the model in order to visually compare the desired and actual cable position. More visual means of examining the subsea situation make it less challenging for both specialists and non-specialists to get an understanding of the cable lay situation during installation. Access to the real-time visualization of the cable laying

operation is not limited to on board crew. Remote personnel and clients can look at a live stream of the real-time model from onshore facilities, allowing them to provide feedback at the moment of scope execution without necessarily being physically present at the vessel. Additional to calculating the cable state in real-time, the model can be used to simulate future cable lay operations by using predicted environmental conditions as input. The mentioned benefits are all opportunities for a reduction of operational costs, failure rates and (in turn) insurance costs. The current work only identifies these opportunities. In order to verify them, follow-up research is required.

10. Conclusions

- Accurately modeling the dynamics of typical export and infield cables during regular cable lay in relatively shallow waters does not require the following physics: tangential hydrodynamic drag, axial stiffness, direct effect of waves, vessel sailing during cable lay, paying out cable during cable lay, aerodynamic drag, torque moments and structural damping. Physics which are not self-evident to be included but should be included are: normal hydrodynamic drag, added mass and bending stiffness.
- For dynamic results with sufficient accuracy the discretization refinement should be $l_0 = 1.55m$ or smaller. For static cases a discretization refinement of $l_0 = 3.10m$ suffices for accurate results.
- The computer system on which the real-time model results have been generated limits the axial stiffness which can be modeled for specific numerical cable element lengths, in order to ensure numerical stability. This is not a problem as modeling an axial stiffness which is workable in the real-time model (which is 4% of the cable's actual EA for $l_0 = 1.55m$) results in a maximum dynamic tension error of 2% in a relatively severe seastate. Therefore it is concluded that the real-time model is capable of accurately modeling the dynamics of typical export and infield cables.
- The executed analytical verification of static model results and validation of dynamic model results prove that the numerical solution is implemented correctly.
- The created model approaches real-time with a negligible delay of several milliseconds while being capable of accurately modeling cable dynamics with an explicit method, inclusion of axial stiffness and a fixed timestep.
- The current work enables the visualization of the real-time model in AR. Successful practical implementation enables the user to look through the water during offshore cable lay operations. This innovation is associated with various opportunities.

11. Recommendations

- The current work uses an explicit method, making the model conditionally stable. Implementation of an implicit method might be worthwhile as this will result in an unconditionally stable model. Using an implicit method, the amount of time steps will decrease as implicit methods permit larger time steps. This advantage is counter-balanced by a higher computational expense per time step. The condition for modeling in real-time given by Equation 29 should still be met, might an implicit method be used. In

order to verify whether real-time modeling is achievable using an implicit method, the implementation of an implicit method and a performance analysis of the resulting model are recommended. It should be noted that for the implementation of an implicit method either an implicit ODE solver should be build or a C# math library (other than the Math.NET Numerics library) which contains an implicit ODE solver should be used.

- The current work assumes the seabed to be frictionless and models the seabed as a distributed visco-elastic support in order to avoid complex formulae for cable-seabed interaction. The mentioned assumption and motivation are in line with [Pinto, 1995]. As outlined by [Randolph and Quiggin, 2009], seabed contact of catenary-shaped lines is often modeled using simple seabed contact models. In order to improve the current work it is recommended to model the seabed using the non-linear hysteretic seabed model developed by [Randolph and Quiggin, 2009]. The recommended model has been validated with field-scale experiments, which showed reasonable accuracy. Therefore it is assumed that the implementation of the recommend model results in a reasonably accurate representation of the physics which occur during cable-seabed interaction.
- Discretization errors can be reduced by applying a non-uniform mesh, where the mesh should be refined in regions where the physical solution has large gradients [Hulshoff, 2016]. It is not expected that a non-uniform mesh affects model stability, because the smallest element in the structure sets the time step for the whole structure [Gravouil and Combescure, 2001].
- In order to reduce the effect of the observed touch-down compression waves, two recommendations are formulated. Damping in tangential direction can prevent the compression waves from traveling from TDP to the system boundaries. Suggestions are structural damping, tangential hydrodynamic damping, seabed shear friction or a combination of these. Another recommendation is to model the cable as inextensible and compare the differences of the resulting model with the current model. Modeling the cable as inextensible might require a thorough re-design of the model. It should be noted that for deeper waters, the error resulting from modeling the cable as inextensible increases. Might it be desired to model the cable as inextensible, the work done by [Newmark, 1959] is a good starting point.
- As added mass significantly affects the dynamic model results, a thorough investigation of its origin and its consequences is recommended. It is likely that such an investigation involves an in-depth analysis of VIV behaviour.
- The current work assumes that the modeled cable has a contra-helical (i.e. torque balanced) armour, which is why torque moments are neglected in the current work. Additionally, axial-torsional effects are expected to only be of influence for local stability of the cable while the current work focuses on the global cable state. Local instability can cause looping, which is a frequent cause of cable damage. Therefore, analysis of the local stability might be worthwhile. If a cable with a helical armour has to be modeled and local stability is of concern, a more in-depth analysis of coupled axial-torsional effects is recommended. Might such research be initiated, the work of [Witz and Tan, 1992] is a good starting point.

- As lateral currents can cause significant lateral movements of the TDP it is recommendable to add a dimension to the proposed model, making it three-dimensional. An extra dimension yields an extra degree of freedom for each node, thereby increasing the size of the state vector with 50%. The expected increase of \bar{t}_{CPU} is therefore 50%, further limiting the range of EA values which can be modeled.
- The assumption that direct wave effects can be neglected is based on assumptions made in [Pinto, 2007]. Verification of this assumption by executing a sensitivity analysis for various seastates in- and excluding the direct effect of waves is recommended. Might this analysis be initiated, a Froude-Krilov force should be added to the physical system. It is expected that the assumption of negligible direct wave effects is valid up to a specific significant wave height.
- The presented discretization error analysis and validation have been executed using $A_{displ} = 0.5m$ hence $H = 1m$. In these dynamic cases no compression occurs. It is recommended to extend these dynamic analyses to higher wave heights in order to verify the model results when compression occurs. Additionally it is recommended to execute the mentioned analyses and the sensitivity analysis on modeling a lower EA for irregular waves instead of harmonic waves, as higher tensions are expected for irregular waves.
- It is expected that coefficient $\hat{\beta}_{l_0}$ can be calculated by executing a *von Neumann stability analysis*. This discards the need for empirically finding $\hat{\beta}_{l_0}$. The work of [Felippa, 2004] is recommended for such scope.
- In the case that the found dynamic tension error of 2% resulting from modeling a lower EA than the actual cable EA for $H = 2.5m$ is deemed unacceptable, a computer with better specifications than the computer specified in Appendix A.3 is recommended.
- In order to successfully implement the proposed innovation in practice the following implementation plan is advised. First of all the working principles of the innovation should be tested in a small-scale set-up. The AR interface might need some revisions by trial-and-error. Subsequently the innovation should be validated on full scale with an actual cable lay vessel. As the required measurement systems are typically on board of a cable lay vessel, the capital investment is expected to be minimal. Finally the identified opportunities associated to the innovation can be verified in an actual offshore cable installation project. The potential legal issues identified during the collaboration with Tilburg University should be kept in mind [Geer et al., 2017].

12. Acknowledgements

I would like to show my gratitude to my supervisor from Tideway Offshore Solutions, Ir. S. Meijer. I would like to thank him for the many energetic meetings we had in which he truly put his mind to work in order to solve the challenges ahead of me. I never returned from meetings with him empty-handed. He unlocked a lot of opportunities for me like access to an actual pair of AR glasses and presenting my thesis at two conferences. He always made sure that I got access to the required information within Tideway - either he answered my questions himself or he guided me towards the right person.

Many thanks to my university supervisor, Dr.ir. P.R. Wellens. When I came to him with the question if he wanted to guide

me during my graduation, the subject of which I made up independently of the university, he was keen on helping me. He has been guiding me throughout my extensive learning experience with the right criticism at the right time, resulting in a better end product.

I would like to thank the chairman of my thesis committee, Prof.dr.ir. A.P. van 't Veer, who always provided very useful and practical feedback.

Many thanks to the students from Tilburg University who joined the Tideway-TILT Clinic: Jaime Geer, Lisette Gotink, Kirill Khotulev and Yusuf Muzak. It was a fruitful learning experience to work with them and the collaboration resulted in an invaluable report about aspects of my research I could not have answered myself. Also I would like to show my gratitude to T. Crepax, who guided us as supervisor from Tilburg University.

Many thanks to C. Keijdener from TU Delft for his essential advice when I was seeking answers on how to model cable dynamics.

I would like to express my sincere gratitude to Tideway Offshore Solutions in general for their financial support and the provided access to their valuable resources. The help from all of my Tideway colleagues is deeply appreciated.

Finally I would like to specially thank my parents and my girlfriend, who have been supporting me continuously during all phases of my graduation project.

References

- J. Azcona, X. Munduate, L. Gonzalez, and T. A. Nygaard. Experimental validation of a dynamic mooring lines code with tension and motion measurements of a submerged chain. *Ocean Engineering*, 129(February 2016):415–427, 2017.
- Bloomberg. AR/VR Is Fourth Wave of Technology: Digi-Capital Founder - Bloomberg, 2016. URL <https://www.bloomberg.com>.
- H. J. J. V. D. Boom. Dynamic Behaviour of Mooring Lines. *Behaviour of Offshore Structures*, pages 359–368, 1985.
- J. Burgess. Bending Stiffness in a Simulation of Undersea Cable Deployment. *International Journal of Offshore and Polar Engineering*, 3(3):197–204, 1993.
- CodaOctopus. The most advanced real time 3D sonar in the world, 2017a.
- CodaOctopus. Echoscope Application Notes - Cable Lay Operations, 2017b.
- R. R. Craig Jr. and A. J. Kurdila. *Fundamentals of Structural Dynamics - Second Edition*. John Wiley & Sons, Inc., 2006.
- DAQRI. Smart Glasses, 2017. URL <https://daqri.com>.
- DHL Trend Research. Augmented reality in logistics. Technical report, 2014. URL <http://www.dhl.com>.
- Digi-Capital. After mixed year, mobile AR to drive \$108 billion VR/AR market by 2021 — Digi-Capital, 2017a. URL <http://www.digi-capital.com>.
- Digi-Capital. Record \$2.3 billion VR/AR investment in 2016 — Digi-Capital, 2017b. URL <http://www.digi-capital.com>.
- DNV. Influence of Pressure in Pipeline Design: Effective Axial Force. *Omae*, (Omae):1–8, 2005.
- DNV. Environmental conditions and environmental loads - DNV-RP-C205. Technical Report April, DNV, 2007.
- DNV GL. Guideline for Installation of Rigid and Flexible Pipelines, Umbilicals and Subsea Power Cables – Analyses. Technical report, DNV GL, 2015.
- DNV GL. Environmental conditions and environmental loads. Technical Report August, DNV, 2017.
- S. Erickson. Microsoft HoloLens enables thyssenkrupp to transform the global elevator industry - Microsoft Devices Blog, 2016. URL <https://blogs.windows.com>.
- European Commission. Proposal for a Directive of the European Parliament and of the Council on the promotion of the use of energy from renewable sources. 0382, 2016.
- EWEA. Wind energy scenarios for 2030. *Ewea*, (July):1–8, 2015. URL <http://www.ewea.org>.
- EWEA / Wind Europe. The European offshore wind industry - Key trends and statistics 2016. 2016. URL <http://www.ewea.org>.
- O. Faltinsen. Sea loads on ships and offshore structures, 1990. URL <https://books.google.com>.
- D. Farber. The next big thing in tech: Augmented reality - CNET, 2013. URL <https://www.cnet.com>.
- C. Felippa. *Introduction to Stability Theory - ASEN 5519-006: Fluid-Structure Interaction*. University of Colorado Boulder, 2004.
- J. H. Ferziger and M. Peric. *Computational Methods for Fluid Dynamics*. 2002.
- A. Frieria, F. Roces, and H. Alloy. Factory of the future, 2016. URL <http://www.airbusgroup.com>.
- GCube. Down to the wire. Technical report, 2016.
- J. Geer, L. Gotink, K. Khotulev, and Y. Muzak. Tideway – TU Delft TILT Clinic: The Use of Augmented Reality in Offshore Subsea Contracting. Technical report, Tilburg University, Tilburg, 2017.
- A. Gravouil and A. Combescure. Multi-time-step explicit–implicit method for non-linear structural dynamics. *International Journal for Numerical Methods in Engineering*, 50(1):199–225, 2001.
- N. Hodge. Power under the sea. pages 26–29, 2014.
- T. J. R. Hughes and W. K. Liu. Implicit-Explicit Finite Elements in Transient Analysis: Stability Theory. *Journal of Applied Mechanics*, 45(2):371, 1978. URL <http://appliedmechanics.asmedigitalcollection.asme.org>.
- S. Hulshoff. *AE2220 II Computational Modelling*. Delft University of Technology, 2016.
- IEEE Standards Association. Augmented Reality in the Oil/Gas/Electric Industry. (June):1–5, 2016. URL <https://standards.ieee.org>.
- Industry. BBC Frozen Planet Augmented Reality - created by INDE - YouTube, 2013. URL <https://www.youtube.com>.
- J. Journee and W. Massie. *Offshore Hydromechanics*. Number January. Delft University of Technology, 2001.
- M. Kaster. Augmented reality is an industry game-changer — Energy Global, 2016. URL <https://www.energyglobal.com>.
- C. Keijdener and A. Jarquin-Laguna. Lecture slides 2017/2018 - Introduction to Computational Dynamics for Offshore structures. Technical report, Delft University of Technology, Delft, 2017.
- W. Lacarbonara and A. Pacitti. Nonlinear modeling of cables with flexural stiffness. *Mathematical Problems in Engineering*, 2008, 2008.
- D. Lavrinc. Tomorrow's Cargo Ships Will Use Augmented Reality to Sail the Seas — WIRED, 2014. URL <https://www.wired.com>.
- S. LI. Mixed Reality-based Interactive Technology for Aircraft Cabin Assembly. *Chinese Journal of Mechanical Engineering*, 22(03):403, 2009. URL <http://www.cjmenet.com>.
- C. Lo. Is augmented reality an offshore game-changer? - Offshore Technology, 2016. URL <http://www.offshore-technology.com>.
- Matlab. Vectorization, 2017. URL <https://nl.mathworks.com>.
- J. McKenna. Experience is key to reduce cable claims, 2012. URL <http://www.windpowermonthly.com>.
- Medium. DAQRI SMART GLASSES SHIP TO CUSTOMERS, 2017. URL <https://medium.com>.
- A. Metrikine and A. Vrouwenvelder. Structural Dynamics; Part 1 and 2. Technical report, Delft University of Technology, 2016.
- MIT. Under , Over and Critical Damping. Technical report, MIT OpenCourseWare, 2011.
- P. Mougins and S. Ducasse. Oopal. *Proceedings of the 18th ACM SIGPLAN conference on Object-oriented programming, systems, languages, and applications - OOPSLA '03*, (November 2003):65, 2003. URL <http://portal.acm.org>.
- N. Newmark. A Method of Computation for Structural Dynamics, 1959.
- Orcina Ltd. OrcaFlex documentation - Version 10.1e, 2017. URL <https://www.orcina.com>.
- W. T. Pinto. On the Dynamics of Low Tension Marine Cables. (January), 1995.
- W. T. Pinto. On the unsteady dynamic response of telecommunication submarine cables during deployment. (Diname), 2007.

- M. Randolph and P. Quiggin. Non-linear hysteretic seabed model for catenary pipeline contact. *International Conference on Offshore Mechanics and Arctic Engineering*, pages 1–10, 2009. URL <http://proceedings.asmedigitalcollection.asme.org>.
- REN21. Renewables 2016: Global Status Report. Technical report, Renewable Energy Policy Network for the 21st Century (REN21), 2016. URL <http://www.ren21.net>.
- C. Ruegg, M. Cuda, and J. Van Gael. Runge-Kutta - ODE Solver Algorithms - MathNET Numerics documentation, 2017. URL <https://numerics.mathdotnet.com>.
- E. Samset, D. Schmalstieg, J. Vander Sloten, A. Freudenthal, J. Declerck, S. Casciaro, Ø. Rideng, and B. Gersak. Augmented reality in surgical procedures. *International Society for Optics and Photonics*, 2008. URL <http://proceedings.spiedigitallibrary.org>.
- Z. Tan, P. Quiggin, and T. Sheldrake. Time domain simulation of the 3D bending hysteresis behaviour of an unbonded flexible riser. 2007.
- Tideway Offshore Solutions. Guideline cable lay operations. Technical report, Breda, 2016.
- K. Vikestad, J. K. Vandiver, and C. M. Larsen. Added mass and oscillation frequency for a circular cylinder subjected to vortex-induced vibrations and external disturbance. *Journal of Fluids and Structures*, 14(7):1071–1088, 2000. URL <http://www.sciencedirect.com>.
- B. Vroegop. Volkswagen MARTA: augmented reality-app voor automonteurs, 2013. URL <http://www.iculture.nl>.
- J. Wagenaar and P. J. Eecen. Current Profiles at the Offshore Wind Farm Egmond aan Zee. Technical Report November, Energy research Centre of the Netherlands (ECN), 2010.
- J. Witz and Z. Tan. On the axial-torsional structural behaviour of flexible pipes, umbilicals and marine cables. *Marine Structures*, 5(2-3):205–227, jan 1992. URL <http://www.sciencedirect.com>.
- N. Yang, D.-s. Jeng, and X. L. Zhou. Tension Analysis of Submarine Cables During Laying Operations. *Elsevier*, pages 282–291, 2013.
- E. Zajac. Dynamics and Kinematics of the Laying and Recovery of Submarine Cable. *The Bell System Technical Journal*, 1957.

A. Appendices

A.1. Force components of normal hydrodynamic drag

The explanation of how the normal hydrodynamic drag is calculated from Section 2.5.1 is continued in the current appendix. Angle θ is calculated using Equation 91.

$$\theta = \text{atan}\left(\frac{\Delta x}{\Delta z}\right) \quad (91)$$

The x - and z -components of the normal hydrodynamic drag force are calculated using Equations 92 and 93. The sign of V_p disappears when this term is squared in Equation 3. To apply $F_{D,n,x}$ and $F_{D,n,z}$ in the correct direction the sign of V_p is applied by the term $\frac{V_p}{|V_p|}$ in Equations 92 and 93.

$$F_{D,n,x} = -F_{D,n} \cdot \cos(\theta) \cdot \frac{V_p}{|V_p|} \quad (92)$$

$$F_{D,n,z} = F_{D,n} \cdot \sin(\theta) \cdot \frac{V_p}{|V_p|} \quad (93)$$

A.2. Typical power cable properties

The current appendix provides data about subsea cables used in offshore wind farms. Section A.2.1 gives the data of cable A , which has been the example cable throughout the current work. Data about typical export and infield cables is given in Section A.2.2.

A.2.1. Cable A

Typically, a subsea power cable manufacturer provides a bending stiffness range instead of a unique value. This is because bending stiffness is dependent on the actual internal friction in the cable. For typical subsea export cable A , a most probable unique value for bending stiffness was chosen after validation with catenary shapes found in real-life cable lay projects. This is *Bending stiffness (prob.)* from Table 6 and this value is used for the bending stiffness of cable A throughout the current work.

Table 6: Subsea power cable A properties.

Input variable	Symbol	Value	Unit
Axial stiffness	EA	556	MN
Submerged mass	m_{sub}	43.92	kg/m
Mass in air	m	88	kg/m
Outer diameter	D	234	mm
Max. allow. tension	T_{max}	195	kN
Min. allow. tension	T_{min}	0	kN
Max. bending radius	MBR	3.6	m
Bending stiffness (min.)	EI	50	$kN.m^2$
Bending stiffness (max.)	EI	710	$kN.m^2$
Bending stiffness (prob.)	EI	300	$kN.m^2$

A.2.2. Typical export and infield cables

Based on Tideway’s cable database, typical values for outer diameter D and axial stiffness EA have been determined for two types of cables: export cables which connect offshore wind farms to the shore and infield cables which connect individual wind turbines with each other within an offshore wind farm. Typical cable properties are presented in Table 7.

Table 7: Typical export and infield cable properties. Average, standard deviation, minimum and maximum values are given for D and EA .

Variable	Export	Infield	Unit
D_{avg}	216.9	133.3	mm
D_{SD}	31.5	16.3	mm
D_{min}	91	102	mm
D_{max}	273	161	mm
EA_{avg}	699.3	277.5	MN
EA_{SD}	204.0	138.9	MN
EA_{min}	400	17.5	MN
EA_{max}	1074	578	MN

A.3. Author’s computer specifications

All real-time model results shown throughout the current work have been generated on the author’s personal computer. The specifications of this computer are given below.

System model and type

HP EliteBook 8560w, x-64 based PC

Processor

Intel(R) Core(TM) i7-2630QM CPU @ 2.00GHz, 2001 Mhz, 4 Cores, 8 Logical processors

Installed Physical Memory (RAM)

8.00 GB

Graphics card

NVIDIA Quadro 1000M

Disk drive

Samsung SSD 840 EVO 250GB

Operating system

Microsoft Windows 10 Home

A.4. Status quo of AR

AR is defined as the expansion of physical reality by adding layers of computer-generated information to the real environment [DHL Trend Research, 2014]. Typical AR hardware platforms are shown in Figure 57.



Figure 57: Different AR hardware platforms. Clockwise from top left: stationary AR [Industry, 2013], handheld AR [Vroegop, 2013], heads-up display [Lavrinc, 2014], wearable AR [Erickson, 2016].

Investors see AR as the fourth wave of technology after computers, the Internet and mobile devices [Bloomberg, 2016]. Experts think that AR might be the next mass market to evolve and that it will be *the next big thing* in the consumer, medical, mobile, automotive and manufacturing markets [Farber, 2013]. A cumulative amount of \$700 million was invested in Virtual Reality (VR) and AR, in 2015. In 2016, these investments reached a record of \$2.3 billion, yielding an investment growth of 300% in one year. Companies taking the lead in terms of investing in VR and AR include Facebook, Google, Apple, Microsoft and Intel [Digi-Capital, 2017b]. In terms of market worth, the AR market grew to \$1.2 billion (in revenues) in 2016 and is expected to reach a worth of \$83 billion by 2021. This explosive increase in market value is partly due to the overall expected growth of the VR / AR market and partly due to AR's share gain over VR's share [Digi-Capital, 2017a]. The AR market growth is visualized in Figure 58.

The explosive growth of the AR market as shown in Figure 58 is expected to accelerate the development of the technological maturity of the technology. This enlarges the range of applications for AR and simplifies its entrance in conservative industries like the offshore industry.

AR Applications are currently already found across various industries. One example of this is found in the aircraft industry. Assembly of aircraft cabins is one of the major bottlenecks in the entire aircraft manufacturing process. The efficiency of the aircraft assembly is enhanced by augmenting the physical world of the worker with useful information like object parameters and 3D assembly instructions [LI, 2009]. Airbus uses an AR system like this to decrease required aircraft assembly time, which also enables the user to access a 3D model of the aircraft from any perspective at any time. The system consists of a tablet device,

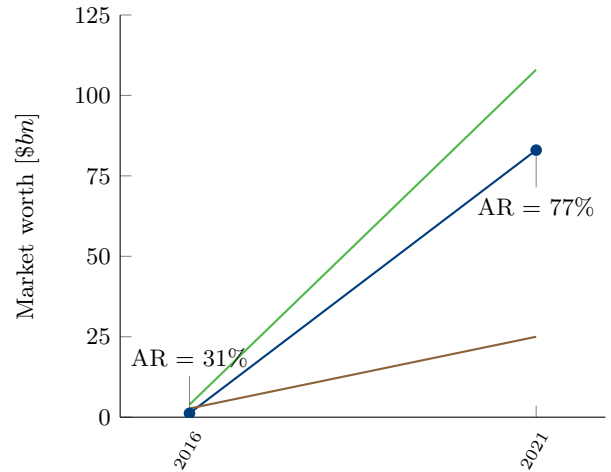


Figure 58: Current VR and AR market worth and expected values [Digi-Capital, 2017a]. Green = VR + AR, blue = AR, brown = VR. Shown AR shares are out of the total VR and AR market.

sensors and customized software. On the A380, it reduces the time to inspect thousands of brackets in the fuselage from three weeks to three days (a factor of five) [Frieria et al., 2016].

In the medical industry AR applications are used since 2008. Incisions are made as small as possible in order to increase the surgery's efficiency, often yielding no direct vision for eye-hand co-ordination for operating personnel. The now booming technology helps by providing visual and sensorial feedback in situations like these, where eye-hand co-ordination is based on e.g. radiological imaging methods [Samset et al., 2008]. During these types of operation, just like during subsea cable laying, a challenge is that one cannot directly see what he or she is doing.

This graduation project is not the only project in which the applicability of AR in the offshore industry is examined. Maersk Oil will use AR at its 2019 North Sea gas production platform 'Culzean' to create safer installations and operations, and to increase efficiencies. Offshore platform workers will have instant access to equipment data and will be able to call in onshore experts for assistance from all around the world, via an AR environment. Experts could be able to virtually monitor and support several offshore locations at once. The company expects AR to have a huge impact on their operations and describes AR as "a powerful component of next-generation digital systems in the offshore oil and gas sector." [Lo, 2016] [Kaster, 2016].

In 2016, the Institute of Electrical and Electronics Engineers published an initiation document about AR in the oil, gas and electric industry with particular focus on wearable AR devices. One of the goals described in this document is to identify existing and missing standards regarding the use of AR in the oil, gas and electric industry. Another goal is to focus on the applications and benefits of AR in these industries, as to create a better understanding of market specific technical needs. Stakeholders in this effort include Shell, BP, Exxon Mobil and various soft- and hardware AR companies [IEEE Standards Association, 2016].